

578262
P. 46

N63-22115

NASA TN D-1963

NASA TECHNICAL NOTE



NASA TN D-1963

EFFECTS OF CROSS-SECTION
SHAPE ON THE LOW-SPEED
AERODYNAMIC CHARACTERISTICS
OF A LOW-WAVE-DRAG
HYPERSONIC BODY

by Bernard Spencer, Jr., and W. Pelham Phillips
Langley Research Center
Langley Station, Hampton, Va.

Reproduced by
NATIONAL TECHNICAL
INFORMATION SERVICE
U.S. Department of Commerce
Springfield, VA 22151

NATIONAL AERONAUTICS AND SPACE ADMINISTRATION • WASHINGTON, D.C. • OCTOBER 1963

REPRODUCED BY
NATIONAL TECHNICAL
INFORMATION SERVICE
U.S. DEPARTMENT OF COMMERCE
SPRINGFIELD, VA. 22151

LIBRARY

Washington 25

40

TECHNICAL NOTE D-1963

EFFECTS OF CROSS-SECTION SHAPE ON THE LOW-SPEED
AERODYNAMIC CHARACTERISTICS OF A
LOW-WAVE-DRAG HYPERSONIC BODY

By Bernard Spencer, Jr., and W. Pelham Phillips

Langley Research Center
Langley Station, Hampton, Va.

NATIONAL AERONAUTICS AND SPACE ADMINISTRATION

NATIONAL AERONAUTICS AND SPACE ADMINISTRATION

TECHNICAL NOTE D-1963

EFFECTS OF CROSS-SECTION SHAPE ON THE LOW-SPEED

AERODYNAMIC CHARACTERISTICS OF A

LOW-WAVE-DRAG HYPERSONIC BODY

By Bernard Spencer, Jr., and W. Pelham Phillips

SUMMARY

An investigation has been made, at low subsonic speeds in the Langley 7- by 10-foot transonic tunnel, to determine the effects on the static longitudinal and lateral aerodynamic characteristics of changing body cross-sectional shape from circular to elliptic on a body having a fineness ratio of 10.00 and designed to have low wave drag at hypersonic speeds. Variations in the cross-section horizontal-axis—vertical-axis ratios from 0.40 to 2.50 were investigated, as well as the effects of body camber for the bodies with horizontal-axis—vertical-axis ratios from 1.00 to 2.50.

Increasing horizontal-axis—vertical-axis ratio indicates that the oval-shaped body of increasing flatness is progressively more efficient in producing lift than the circular-shaped body. The production of drag due to lift is also more efficient for oval-shaped bodies of increasing flatness and results in increased maximum lift-drag ratio as horizontal-axis—vertical-axis ratio is increased.

Changing major-axis—minor-axis ratio with the major axis either horizontal or vertical results in a slight rearward shift in body center of pressure at low angles of attack, as compared with the circular body. Increasing horizontal-axis—vertical-axis ratio resulted in decreasing longitudinal stability.

The use of body camber indicates only small effects of displacing the lift, drag, and pitching-moment curves, with little or no effect on lift-curve slope, longitudinal stability level, maximum lift-drag ratio, or body center-of-pressure location.

For the moment reference point of the present investigation, each of the bodies indicated negative values of static directional stability, with reduction in directional instability accompanying increases in horizontal-axis—vertical-axis ratio. These reductions in directional instability are apparently the same as the decreases in longitudinal stability for the body rotated 90° . The use of negative camber provides a positive increment in directional stability above an angle of attack of 6° .

INTRODUCTION

Experimental and theoretical studies relating to the effects on the longitudinal and lateral aerodynamic characteristics of changing the cross-sectional shape of low-fineness-ratio cones from circular to elliptic have been made at speeds from high subsonic to supersonic. (See refs. 1 to 5.) The results of these investigations have indicated considerable improvement in maximum lift-drag ratio and lift-curve slope. Reference 2 shows that at supersonic speeds reductions in the pressure drag of a cone of given length and base area are realized at low angles of attack as the cross section is changed from circular to elliptic. Little or no aerodynamic information exists, however, for either conical or contoured bodies having variations in cross section at low subsonic speeds. Whereas the low-fineness-ratio bodies have application as possible manned reentry shapes, externally contoured bodies of higher fineness ratio may have application as large-volume fuselages for hypersonic cruise vehicles with horizontal take-off or landing capabilities. Any gain in the performance and lifting capabilities of these fuselages would be reflected in improved take-off and landing characteristics of the configuration.

The present investigation was initiated, therefore, to provide information at low subsonic speeds on the effects on the longitudinal and lateral aerodynamic characteristics of changing body cross-sectional shape from circular to elliptic for a body with an equivalent fineness ratio of 10.00 and designed to have low wave drag at hypersonic speeds. Variations in the cross-section horizontal-axis—vertical-axis ratio from 0.40 to 2.50 were investigated for configurations having constant length and the same longitudinal distribution of cross-sectional area. Included in the investigation are the effects of body camber for the bodies having horizontal-axis—vertical-axis ratios from 1.00 to 2.50. Tests were conducted at a free-stream Mach number of 0.40 corresponding to an average test Reynolds number per foot of approximately 2.51×10^6 . The angle-of-attack range was from approximately -1° to 18° at angles of sideslip of 0° and $\pm 5^\circ$.

SYMBOLS

Longitudinal data are presented about the stability axes, and lateral data are presented about the body axes. All coefficients are nondimensionalized with respect to the projected planform area and maximum diameter of the body with circular cross section. The moment reference point was located longitudinally at 0.667 of the configuration total length and corresponds to the centroid of volume of the bodies. The vertical location of the moment reference for the various bodies is indicated in figure 1.

C_L lift coefficient, $\frac{\text{Lift}}{qS_r}$

| | |
|--|--|
| C_D | drag coefficient, $\frac{\text{Gross drag}}{qS_r}$ |
| C_m | pitching-moment coefficient, $\frac{\text{Pitching moment}}{qS_r d_b}$ |
| C_Y | side-force coefficient, $\frac{\text{Side force}}{qS_r}$ |
| C_n | yawing-moment coefficient, $\frac{\text{Yawing moment}}{qS_r d_b}$ |
| C_l | rolling-moment coefficient, $\frac{\text{Rolling moment}}{qS_r d_b}$ |
| $C_{D,\min}$ | minimum drag coefficient, $C_L \approx 0$ |
| $C_{L\alpha}$ | lift-curve slope, per deg ($\alpha = 0^\circ$) |
| $C_{m\alpha}$ | longitudinal stability parameter, per deg |
| C_N | normal-force coefficient, $\frac{\text{Normal force}}{qS_r}$ |
| $C_{Y\beta} = \frac{\Delta C_Y}{\Delta \beta}$ | per deg, $\beta = 0^\circ$ |
| $C_{n\beta} = \frac{\Delta C_n}{\Delta \beta}$ | per deg, $\beta = 0^\circ$ |
| $C_{l\beta} = \frac{\Delta C_l}{\Delta \beta}$ | per deg, $\beta = 0^\circ$ |
| A | total cross-sectional area of bodies (fig. 3), sq ft |
| a | semimajor axis length of elliptic cross section, ft |
| b | semiminor axis length of elliptic cross section, ft |
| d_b | equivalent base diameter of body, $2\sqrt{ab}$, ft |
| l | configuration total length, ft |
| L/D | lift-drag ratio |

| | |
|-----------------------------|---|
| $(L/D)_{\max}$ | maximum lift-drag ratio |
| P | free-stream static pressure, lb/sq ft |
| P_b | base pressure, lb/sq ft |
| $\frac{\Delta P_b}{q}$ | pressure coefficient at model base, $\frac{P_b - P}{q}$ |
| q | free-stream dynamic pressure, lb/sq ft |
| r | radius of body with $a/b = 1.00$ at any body length, ft |
| r_b | base radius of body with $a/b = 1.00$, ft |
| S_r | projected planform area of body with $a/b = 1.00$, sq ft |
| S_{wet} | total wetted area of bodies (excluding base area), sq ft |
| x | longitudinal coordinate of bodies, ft |
| $\frac{x_{cg}}{l}$ | longitudinal center-of-gravity location |
| $\frac{x_{cp}}{l}$ | longitudinal center-of-pressure location ($\alpha = 0^\circ$), $\frac{x_{cg}}{l} - \frac{\partial C_m}{\partial C_N} \frac{d_b}{l}$ |
| V_x | integrated body volume at x distance from body apex, cu ft |
| α | angle of attack, deg (see fig. 1 for reference lines) |
| β | angle of sideslip, deg |
| ϕ | angle of roll about the body ordinate reference line, deg |
| Configuration designations: | |
| A | circular body, $a/b = 1.00$ |
| B | elliptic body, $a/b = 1.25$ |
| C | elliptic body, $a/b = 1.50$ |
| D | elliptic body, $a/b = 2.00$ |
| E | elliptic body, $a/b = 2.50$ |

Configuration designation subscripts:

- 1 symmetrical bodies, $\phi = 0^\circ$
- 2 negatively cambered bodies, $\phi = 0^\circ$
- 3 positively cambered bodies, $\phi = 0^\circ$
- 4 symmetrical bodies, $\phi = 90^\circ$

MODEL

Drawings of the various bodies used in the investigation are presented in figure 1, with pertinent geometric characteristics shown. Photographs of the uncambered circular body A_1 and the uncambered elliptic body E_1 are presented as figure 2.

The shape of the configurations followed an $x^{2/3}$ power series contour, which represents a low-wave-drag configuration at hypersonic speeds. For the body of revolution (the equivalent body), $r = \frac{r_0}{l^{2/3}} x^{2/3}$ where r represents the radius at various longitudinal stations x . As the configuration cross sections were altered from circular to elliptic, length and cross-sectional-area distribution ($\pi ab = \pi r^2$ at same longitudinal station) were held constant (fig. 3), with resulting increases in body wetted area as a/b increases. For $\phi = 0^\circ$, increasing a/b also results in increased configuration aspect ratio.

The uncambered elliptic bodies were tested at roll angles ϕ of 0° and 90° , with the $\phi = 90^\circ$ condition allowing for testing of bodies having horizontal-axis-vertical-axis ratio less than 1.00. For the cambered bodies of the investigation ($a/b = 1.00$ to 2.50, $\phi = 0^\circ$), the cross sections were oriented normal to a reference line at the intersection of the semiminor axis and the cross-section perimeter. (See fig. 1(a).) Design ordinates for the various uncambered bodies are given in table I.

TESTS AND CORRECTIONS

The present investigation was conducted in the Langley 7- by 10-foot transonic tunnel at a Mach number of 0.40 corresponding to an average test Reynolds number per foot of approximately 2.51×10^6 . The models were sting mounted and forces and moments were measured by means of a six-component strain-gage balance. The bodies were tested through an angle-of-attack range from approximately -1° to 18° at angles of sideslip of 0° and $\pm 5^\circ$. The lateral directional stability derivatives $C_{n\beta}$, $C_{l\beta}$, and $C_{Y\beta}$ were obtained by calculating average slopes

between $\beta = 5^\circ$ and $\beta = -5^\circ$. Boundary-layer transition was allowed to occur freely on the bodies for the tests of the present investigation.

Jet-boundary corrections were found to be negligible and have not been applied to the data. However, solid blockage corrections due to the body and wake blockage corrections were applied as determined by the method outlined in reference 6. The angles of attack and sideslip have been corrected for the effects of sting and balance bending under load.

For this investigation gross drag has been presented, and an integrated rake was used to obtain the average values of base pressure coefficient for each of the bodies. Base pressure variations with angle of attack are presented in figure 4 for each of the bodies tested. The angle-of-attack reference line was taken as the line joining the body apex and the center point of the body base.

RESULTS AND DISCUSSION

Presentation of Results

Figure 5 presents longitudinal aerodynamic characteristics for the cambered and uncambered bodies having $\phi = 0^\circ$ and a/b from 1.00 to 2.50. The effects on the longitudinal aerodynamic characteristics of changing a/b from 2.50 to 1.25 for the symmetrical bodies having $\phi = 90^\circ$ are presented in figure 6. The lateral directional stability derivatives $C_{Y\beta}$, $C_{n\beta}$, and $C_{l\beta}$ are presented in figure 7 for the cambered bodies having a/b from 1.00 to 2.50 and $\phi = 0^\circ$ and in figure 8 for the symmetrical bodies having a/b from 2.50 to 1.00 and $\phi = 90^\circ$. Comparison of the lift, drag, pitching moment, and lift-drag ratio variation with increasing angle of attack for the symmetrical bodies having horizontal-axis-vertical-axis ratio from 0.40 ($a/b = 2.50$, $\phi = 90^\circ$) to 2.50 ($a/b = 2.50$, $\phi = 0^\circ$) are presented in figure 9, with a summary of the aerodynamic parameters $C_{m\alpha}$, $C_{L\alpha}$, $(L/D)_{\max}$, $C_{D,\min}$, $\frac{x_{cp}}{l}$, $C_{n\beta}$, and $C_{Y\beta}$ presented in figure 10.

Longitudinal Aerodynamic Characteristics

For the symmetrical bodies figure 4 shows that changing a/b produced little or no effect on the base pressure variation with angle of attack. The base pressure coefficient varied only between -0.10 and -0.14 for the symmetrical bodies at zero angle of attack (fig. 4) and the variation of $\frac{\Delta p_b}{q}$ with angle of attack was similar for all uncambered bodies. The difference noted in $\frac{\Delta p_b}{q}$ for the negatively and positively cambered bodies at a given angle of attack may be indicative of the presence of induced or increased angle of attack near the body base due to cross-flow effects.

The effects of camber on the lift, drag, and pitching-moment characteristics of the bodies having $a/b = 1.00$ to 2.50 and $\phi = 0^\circ$ are presented in figure 5. Positive camber for the $a/b = 1.00$, $\phi = 0^\circ$ body (fig. 5) results in slight increases in C_L at a given angle of attack, increases in C_D at the higher angles of attack, and a slight negative increment in C_m throughout the angle-of-attack range as compared with results for the uncambered body. The opposite occurs for the negatively cambered body compared with the uncambered body. The small effect of camber on the longitudinal aerodynamic characteristics of the $a/b = 1.00$, $\phi = 0^\circ$ body diminished with increasing a/b as would be expected, since a reduction in the amount of camber of the body occurs with decreases in the vertical axis; however, the measurements do not show increments consistent with the $a/b = 1.00$ body. The small effect of camber is seen to be similar to that of cambered airfoils in displacing the lift, drag, and pitching-moment curves. Only slight effects of camber on the longitudinal aerodynamic parameters C_{L_α} , $C_{D,min}$, $(L/D)_{max}$, C_{m_α} , and $\frac{x_{cp}}{l}$ are noted in figure 10.

The effects on the longitudinal aerodynamic characteristics of changing a/b from 2.50 to 1.00 ($\phi = 90^\circ$) and from 1.00 to 2.50 ($\phi = 0^\circ$) are presented in figure 9. Successive increases in C_L , C_D , and C_m were realized from increasing horizontal-axis—vertical-axis ratio from 0.40 to 2.50 . These increases are primarily a result of increasing the planform area, with secondary effects of increasing the body aspect ratio. Furthermore, it is observed in figure 9(d) from the L/D variation with angle of attack that considerable improvement in $(L/D)_{max}$ is realized by increasing horizontal-axis—vertical-axis ratio, over the entire range, with the rate of increase being largest for $a/b > 1.00$, $\phi = 0^\circ$. These results indicate that oval-shaped bodies of increasing flatness are progressively more efficient in producing lift than are the circular bodies. Similar results have been noted at supersonic speeds for a series of low-fineness-ratio cones (ref. 1).

A summary of the longitudinal aerodynamic characteristics of the symmetrical bodies having variations in a/b ($\phi = 0^\circ$ or $\phi = 90^\circ$) is presented in figure 10. Increases in C_{L_α} from approximately 0.0020 to 0.0075 result from increasing a/b from 1.00 to 2.50 ($\phi = 0^\circ$). As previously mentioned, the largest increases in lift-curve slope are due to the additional planform area. The additional increments in lift-curve slope are realized as a result of the change in aspect ratio, as can be seen from the increases in C_{L_α} over the range of increasing horizontal-axis—vertical-axis ratio of these tests, when C_{L_α} is based on the true projected planform area of each body.

The variation of minimum drag coefficient (fig. 10) for the symmetrical bodies indicates an increasing trend in $C_{D,min}$ with increasing a/b ($\phi = 0^\circ$ or 90°) when the coefficients are based on the circular-body reference area. Increases in $C_{D,min}$ for increasing a/b ($\phi = 90^\circ$) and decreases in $C_{D,min}$ for increasing a/b ($\phi = 0^\circ$) are realized when the coefficients are based on the true body planform area. The fact that the minimum drag coefficients remain essentially constant over the entire a/b range and that $(L/D)_{max}$ continuously

increases for increasing horizontal-axis—vertical-axis ratio indicates that the production of drag due to lift is considerably more efficient for oval-shaped bodies of increasing flatness and is directly related to the aspect-ratio effects as previously mentioned in connection with the lift-curve slope.

The variation of longitudinal stability parameter $C_{m\alpha}$ with a/b indicates increases in destabilizing moment with increases in horizontal-axis—vertical-axis ratio. As a/b increases ($\phi = 0^\circ$ or $\phi = 90^\circ$) the body center of pressure moves rearward. Similar results were observed at supersonic speeds on a series of low-fineness-ratio cones having variation in a/b (ref. 1).

Lateral Directional Characteristics

The effects on the lateral directional characteristics of changing a/b and of the use of body camber for the bodies having $a/b = 1.00$ to 2.50 and $\phi = 0^\circ$ are presented in figure 7. For the moment reference location of the present investigation, each of the bodies indicated negative values of static directional stability at low angles of attack, with the effects of camber being relatively insignificant below an angle of attack of 6° . The values of $-C_{Y\beta}$ and $-C_{n\beta}$ for $\phi = 0^\circ$ at $\alpha = 0^\circ$ are seen to be approximately the same as the values of $C_{L\alpha}$ and $C_{m\alpha}$ for $\phi = 90^\circ$ at $\alpha = 0^\circ$, as would be expected. (See fig. 10.) For the symmetrical bodies, positive $C_{n\beta}$ occurs at the higher angles of attack, with a reduction in the angle at which positive $C_{n\beta}$ occurs accompanying increases in a/b for $\phi = 0^\circ$. For the symmetrical bodies ($\phi = 90^\circ$), this effect is well illustrated in figure 8 where reductions in $-C_{n\beta}$ are noted as horizontal-axis—vertical-axis ratio is increased. Figure 7 indicates that the use of negative camber provides a positive increment in directional stability above an angle of attack of 6° for each of the bodies tested. At angles of attack in excess of 18° , inconsistent repeatability in the lateral derivatives was noted, caused by severe oscillations probably resulting from the formation of a Kármán vortex street alternating from side to side. This effect at high angles of attack has also been indicated for a high-fineness-ratio sharp-nose body at low speeds (ref. 7). Similar results may be expected in pitching-moment variation when the effective angle of attack is extremely high.

Increases in variation of $-C_{l\beta}$ with increasing angle of attack occur as horizontal-axis—vertical-axis ratio is increased (figs. 7 and 8). This effect, when combined with the reduction in $-C_{n\beta}$ realized from increasing horizontal-axis—vertical-axis ratio indicates that oval-shaped bodies of increasing flatness, while improving the overall lift and lift-drag-ratio characteristics, should also improve the dynamic directional characteristics of bodies. Analysis of the effects of roll and yaw on the dynamic directional characteristics of high-performance configurations may be found in reference 8.

CONCLUDING REMARKS

An investigation has been conducted at low subsonic speeds on the effects on the aerodynamic characteristics of changing body cross-sectional shape and the use of body camber for a fineness ratio 10.00, low wave-drag hypersonic body. Results of the investigation may be summarized as follows:

1. Increasing horizontal-axis—vertical-axis ratio indicates that the oval-shaped bodies of increasing flatness are progressively more efficient in producing lift than is the circular body. The production of drag due to lift is also more efficient for oval-shaped bodies of increasing flatness and results in increased maximum lift-drag ratio as horizontal-axis—vertical-axis ratio is increased.
2. Changing major-axis—minor-axis ratio with the major axis either horizontal or vertical results in a slight rearward shift in body center of pressure at low angles of attack, as compared with that for the circular body. Increasing horizontal-axis—vertical-axis ratio results in decreasing longitudinal stability.
3. The use of body camber produces only small effects of displacing the lift, drag, and pitching-moment curves, with little or no effect on lift-curve slope, longitudinal stability level, maximum lift-drag ratio, or body center-of-pressure location.
4. For the moment reference point of the present investigation, each of the bodies indicated negative values of static directional stability, with reduction in directional instability accompanying increases in horizontal-axis—vertical-axis ratio for the symmetrical bodies. These reductions in directional instability are apparently the same as the decreases in longitudinal stability for the body rotated 90° . The use of negative camber provides a positive increment in directional stability above an angle of attack of 6° .

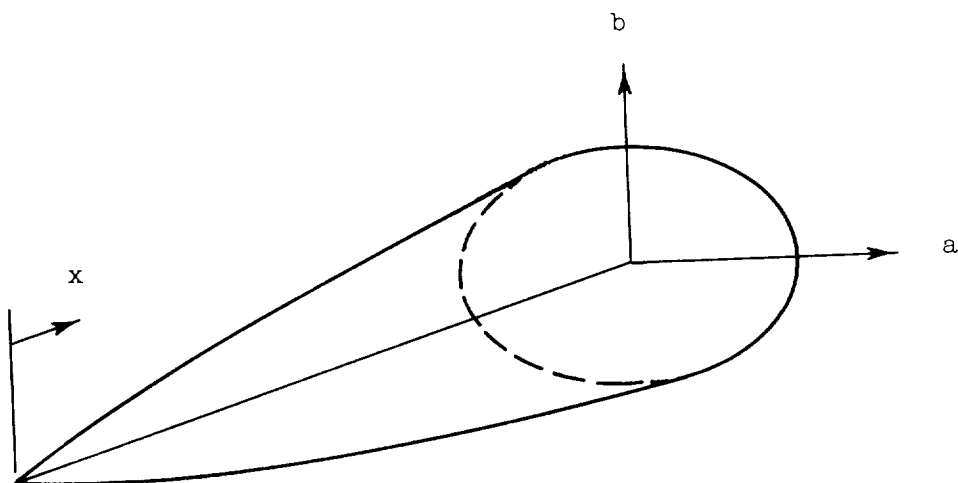
Langley Research Center,
National Aeronautics and Space Administration,
Langley Station, Hampton, Va., June 24, 1963.

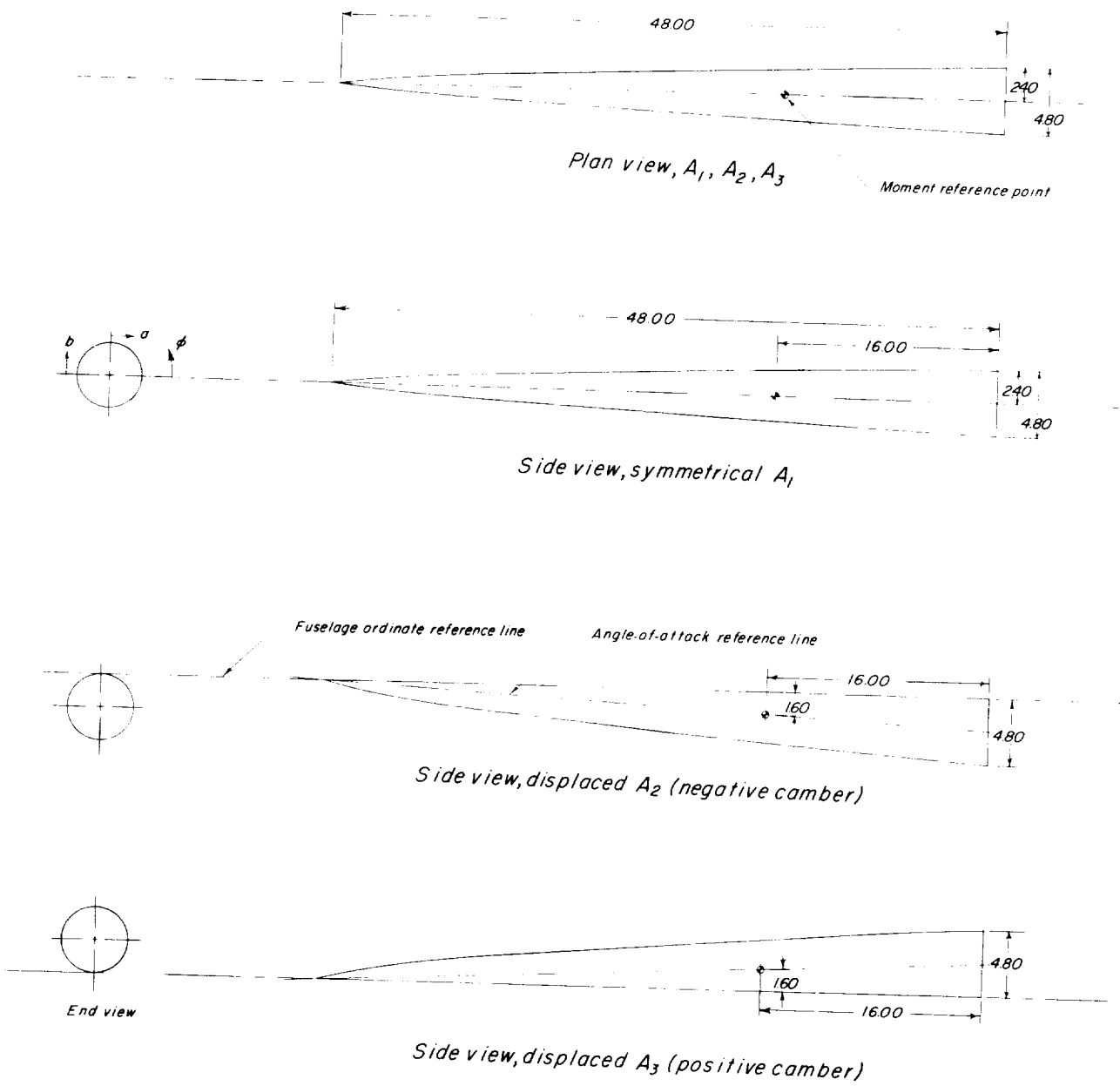
REFERENCES

1. Jorgensen, Leland H.: Elliptic Cones Alone and With Wings at Supersonic Speeds. NASA Rep. 1376, 1958. (Supersedes NACA TN 4045.)
2. Fraenkel, L. E.: Supersonic Flow Past Slender Bodies of Elliptic Cross-Section. R. & M. No. 2954, British A.R.C., 1955.
3. Stivers, Louis S., Jr., and Levy, Lionel L., Jr.: Longitudinal Force and Moment Data at Mach Numbers From 0.60 to 1.40 for a Family of Elliptic Cones With Various Semiapex Angles. NASA TN D-1149, 1961.
4. Seaman, Donna Jean, and Dore, Frank J.: Force and Pressure Coefficients of Elliptic Cones and Cylinders in Newtonian Flow. Rep. No. ZA-7-004, Consolidated Vultee Aircraft Corp., May 16, 1952.
5. Ferri, Antonio: The Linearized Characteristics Method and Its Application to Practical Nonlinear Supersonic Problems. NACA Rep. 1102, 1952. (Supersedes NACA TN 2515.)
6. Herriot, John G.: Blockage Corrections for Three-Dimensional-Flow Closed-Throat Wind Tunnels, With Consideration of the Effects of Compressibility. NACA Rep. 995, 1950. (Supersedes NACA RM A7B28.)
7. Letko, William: A Low-Speed Experimental Study of the Directional Characteristics of a Sharp-Nosed Fuselage Through a Large Angle-of-Attack Range at Zero Angle of Sideslip. NACA TN 2911, 1953.
8. Moul, Martin T., and Paulson, John W.: Dynamic Lateral Behavior of High-Performance Aircraft. NACA RM L58E16, 1958.

TABLE I.- DESIGN BODY ORDINATES FOR UNCAMBERED BODIES

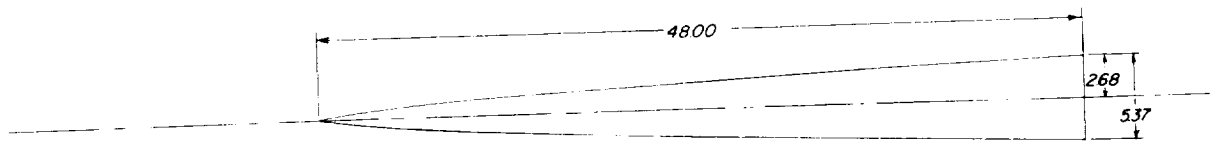
| x, in. | Semimajor-axis—semiminor-axis ratio, a/b | | | | | | | | |
|-----------|--|--------|--------|--------|--------|--------|--------|--------|--------|
| | 1.00 | 1.25 | | 1.50 | | 2.00 | | 2.50 | |
| | r, in. | a, in. | b, in. | a, in. | b, in. | a, in. | b, in. | a, in. | b, in. |
| 0 | 0 | 0 | 0 | 0 | 0 | 0 | 0 | 0 | 0 |
| 2 | .2884 | .3225 | .2580 | .3533 | .2355 | .4079 | .2040 | .4560 | .1824 |
| 4 | .4579 | .5119 | .4096 | .5608 | .3739 | .6475 | .3238 | .72395 | .2896 |
| 6 | .5999 | .6708 | .5367 | .7349 | .4899 | .8485 | .4243 | .9486 | .3795 |
| 8 | .7268 | .8126 | .6501 | .8902 | .5935 | 1.0279 | .5140 | 1.1492 | .4597 |
| 10 | .8434 | .9430 | .7544 | 1.0330 | .6887 | 1.1928 | .5964 | 1.3335 | .5334 |
| 14 | 1.0555 | 1.1801 | .9441 | 1.2928 | .8618 | 1.4927 | .7464 | 1.6689 | .6675 |
| 18 | 1.2480 | 1.3954 | 1.1163 | 1.5286 | 1.0190 | 1.7650 | .8825 | 1.9732 | .7893 |
| 24 | 1.5119 | 1.6904 | 1.3523 | 1.8517 | 1.2345 | 2.1382 | 1.0691 | 2.3904 | .9562 |
| 30 | 1.7544 | 1.9615 | 1.5692 | 2.1488 | 1.4325 | 2.4811 | 1.2406 | 2.7738 | 1.1095 |
| 34 | 1.9070 | 2.1322 | 1.7058 | 2.3357 | 1.5571 | 2.6970 | 1.3485 | 3.0152 | 1.2061 |
| 38 | 2.0538 | 2.2963 | 1.8371 | 2.5155 | 1.6770 | 2.9046 | 1.4523 | 3.2473 | 1.2989 |
| 42 | 2.1456 | 2.4548 | 1.9638 | 2.6891 | 1.7927 | 3.1050 | 1.5525 | 3.4714 | 1.3886 |
| 44 | 2.2647 | 2.5321 | 2.0257 | 2.7738 | 1.8492 | 3.2028 | 1.6014 | 3.5807 | 1.4323 |
| 46 | 2.3328 | 2.6082 | 2.0866 | 2.8572 | 1.9048 | 3.2992 | 1.6496 | 3.6884 | 1.4754 |
| 48 | 2.4000 | 2.6833 | 2.1466 | 2.9394 | 1.9596 | 3.3941 | 1.6971 | 3.7946 | 1.5178 |



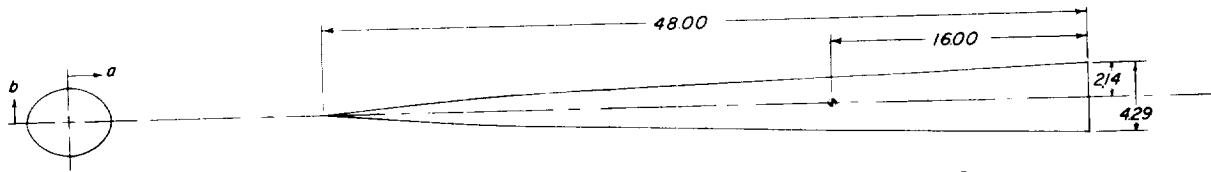


(a) Bodies of revolution A_1, A_2, A_3 ; $a/b = 1.00$.

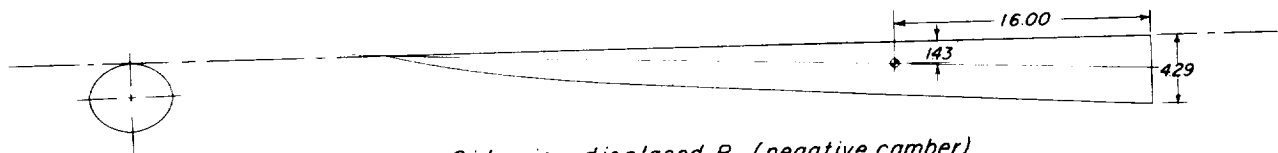
Figure 1.- Geometric characteristics of various bodies of present investigation. Positive directions for a , b , and ϕ are indicated by arrows. All dimensions are in inches unless otherwise noted.



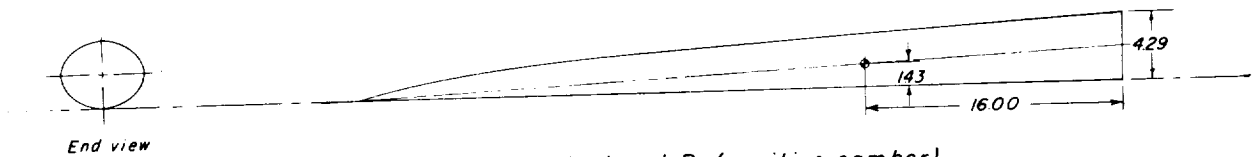
Plan view, B_1, B_2, B_3 ; Side view, B_4



Side view, symmetrical B_1 ; Plan view, B_4



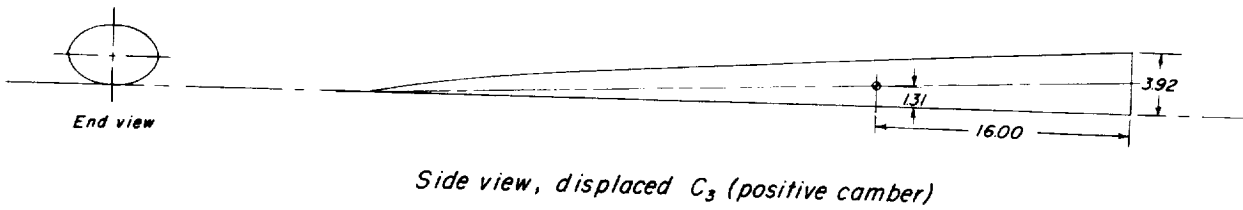
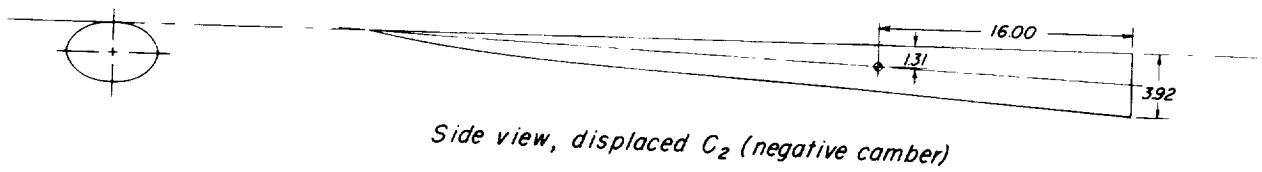
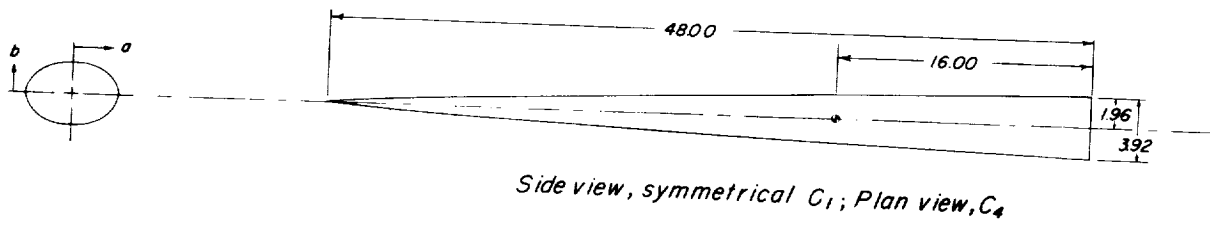
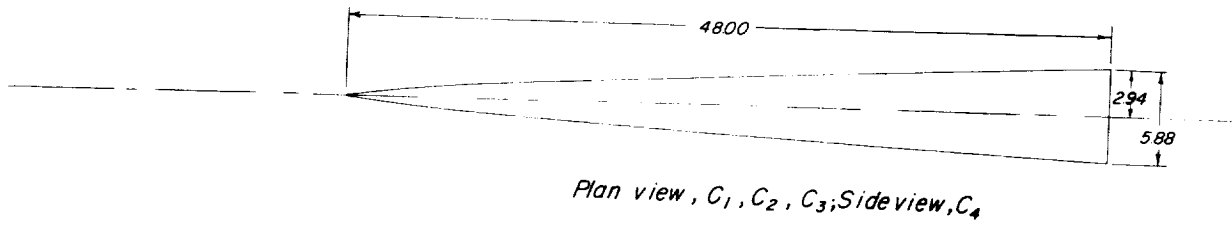
Side view, displaced B_2 (negative camber)



Side view, displaced B_3 (positive camber)

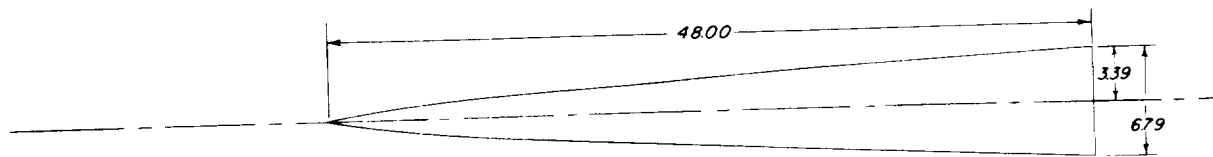
(b) Elliptic bodies B_1, B_2, B_3, B_4 ; $a/b = 1.25$.

Figure 1.- Continued.

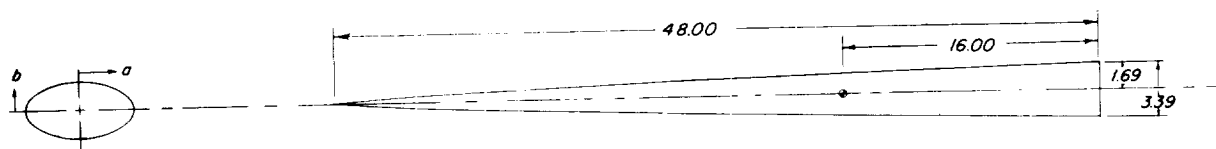


(c) Elliptic bodies C_1, C_2, C_3, C_4 ; $a/b = 1.50$.

Figure 1.- Continued.



Plan view, D_1, D_2, D_3 ; Side view, D_4



Side view, symmetrical D_1 ; Plan view, D_4



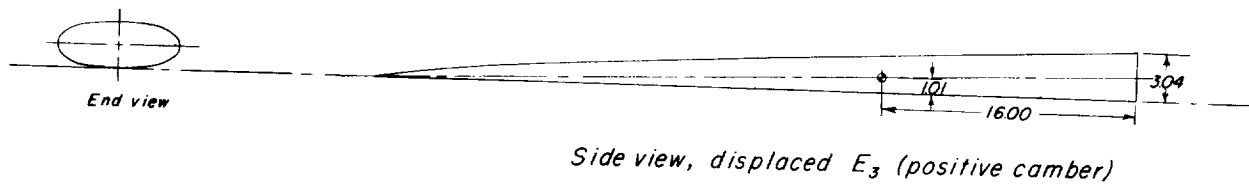
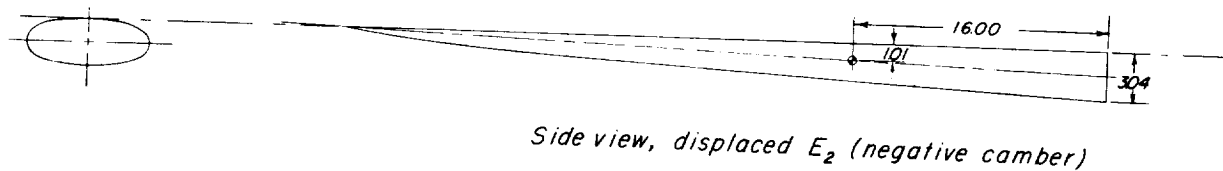
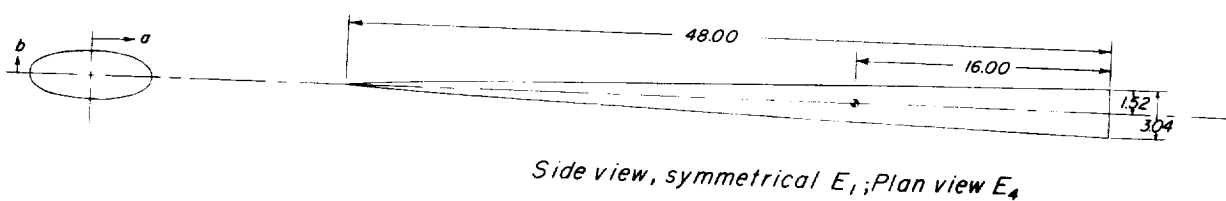
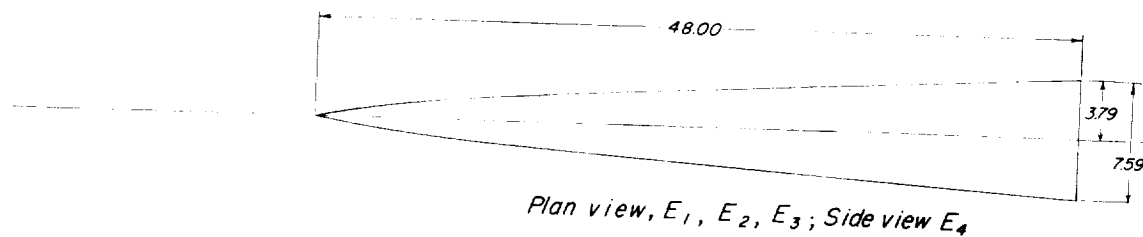
Side view, displaced D_2 (negative camber)



Side view, displaced D_3 (positive camber)

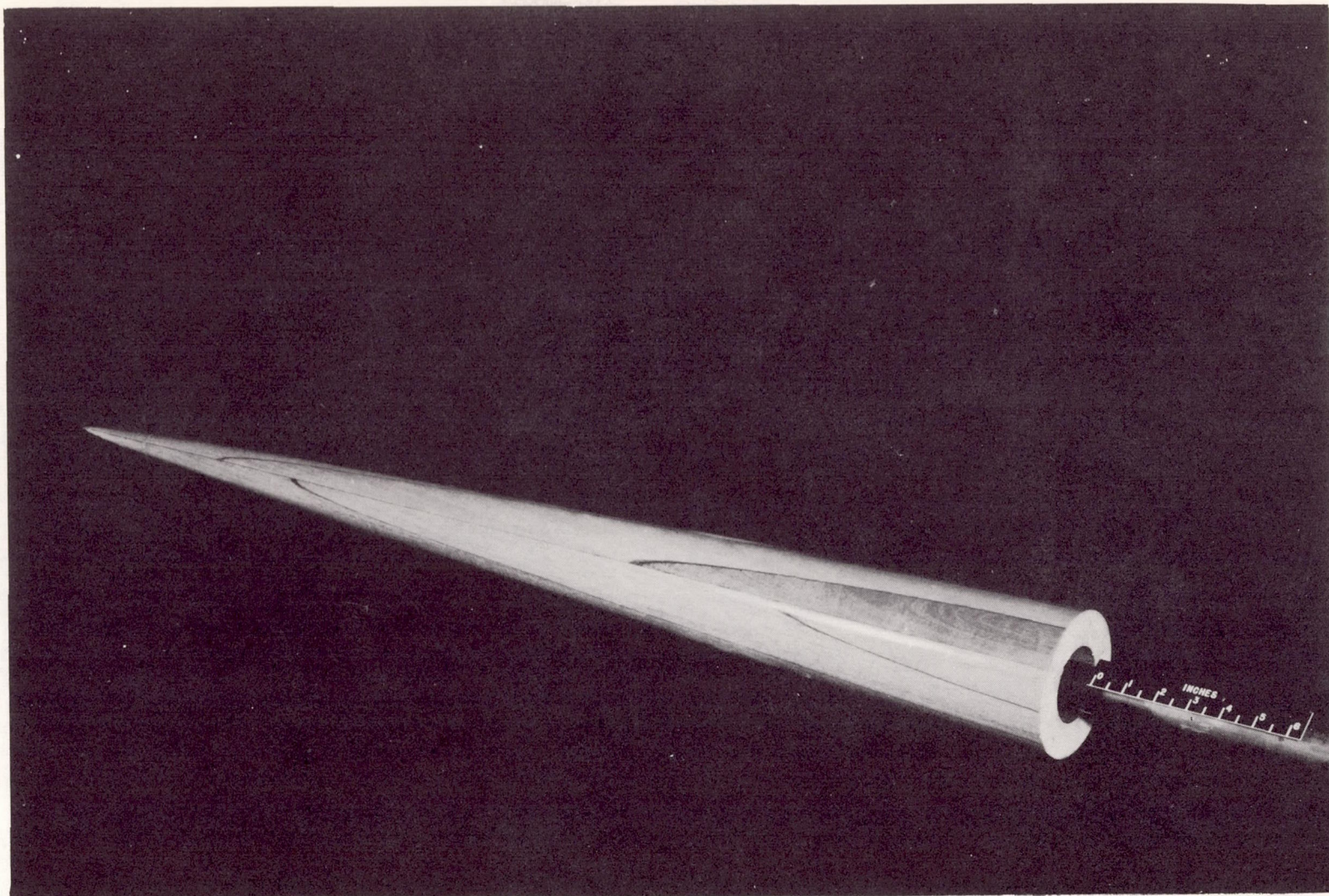
(d) Elliptic bodies D_1, D_2, D_3, D_4 ; $a/b = 2.00$.

Figure 1.- Continued.



(e) Elliptic bodies E_1, E_2, E_3, E_4 ; $a/b = 2.50$.

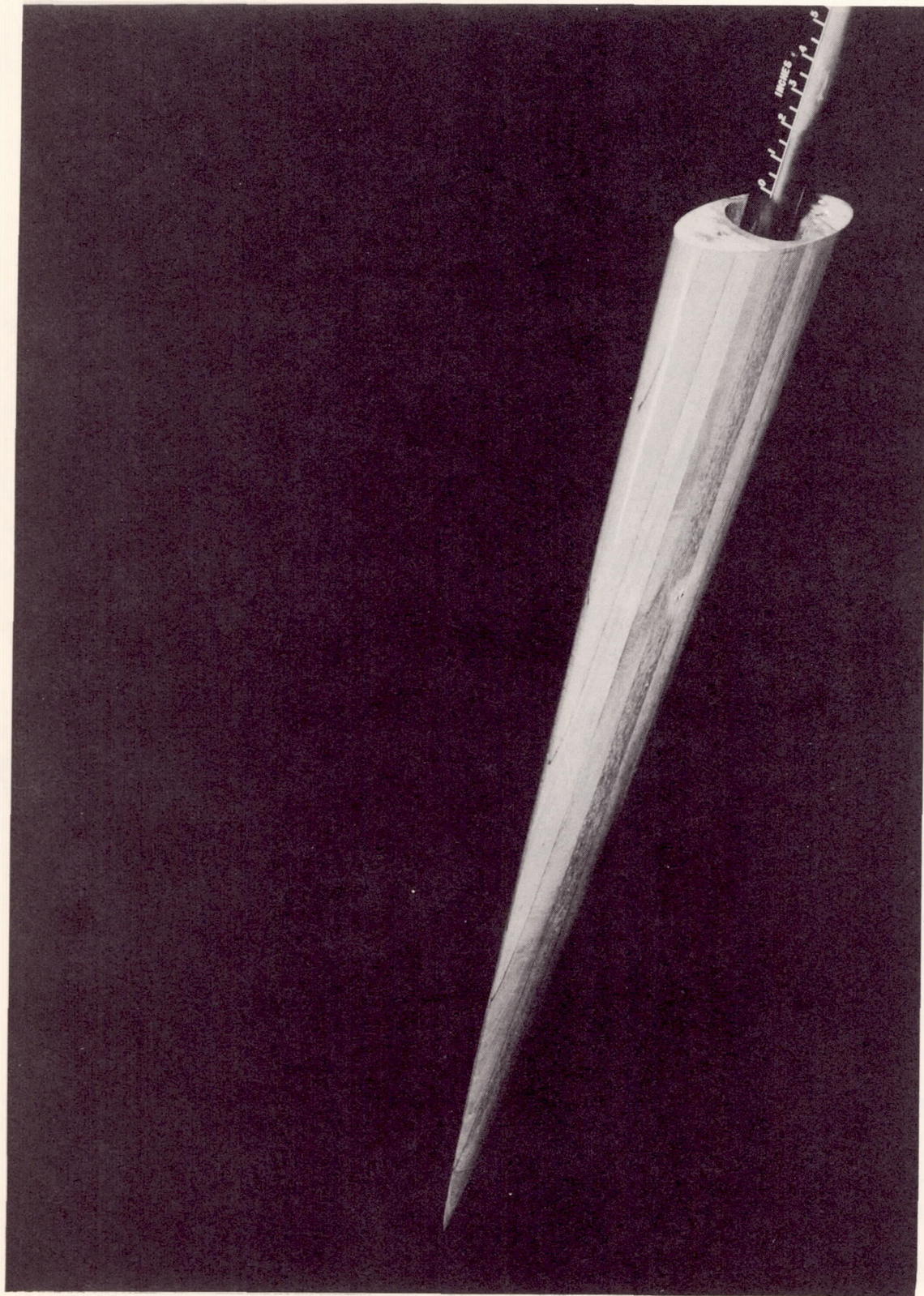
Figure 1.- Concluded.



(a) Model A_1 ; $\phi = 0^\circ$; $a/b = 1.00$.

L-62-5683

Figure 2.- Body of revolution and elliptic body mounted in Langley 7- by 10-foot transonic tunnel.



(b) Model E_1 ; $\phi = 0^\circ$; $a/b = 2.50$.

Figure 2.- Concluded.

L-62-5684

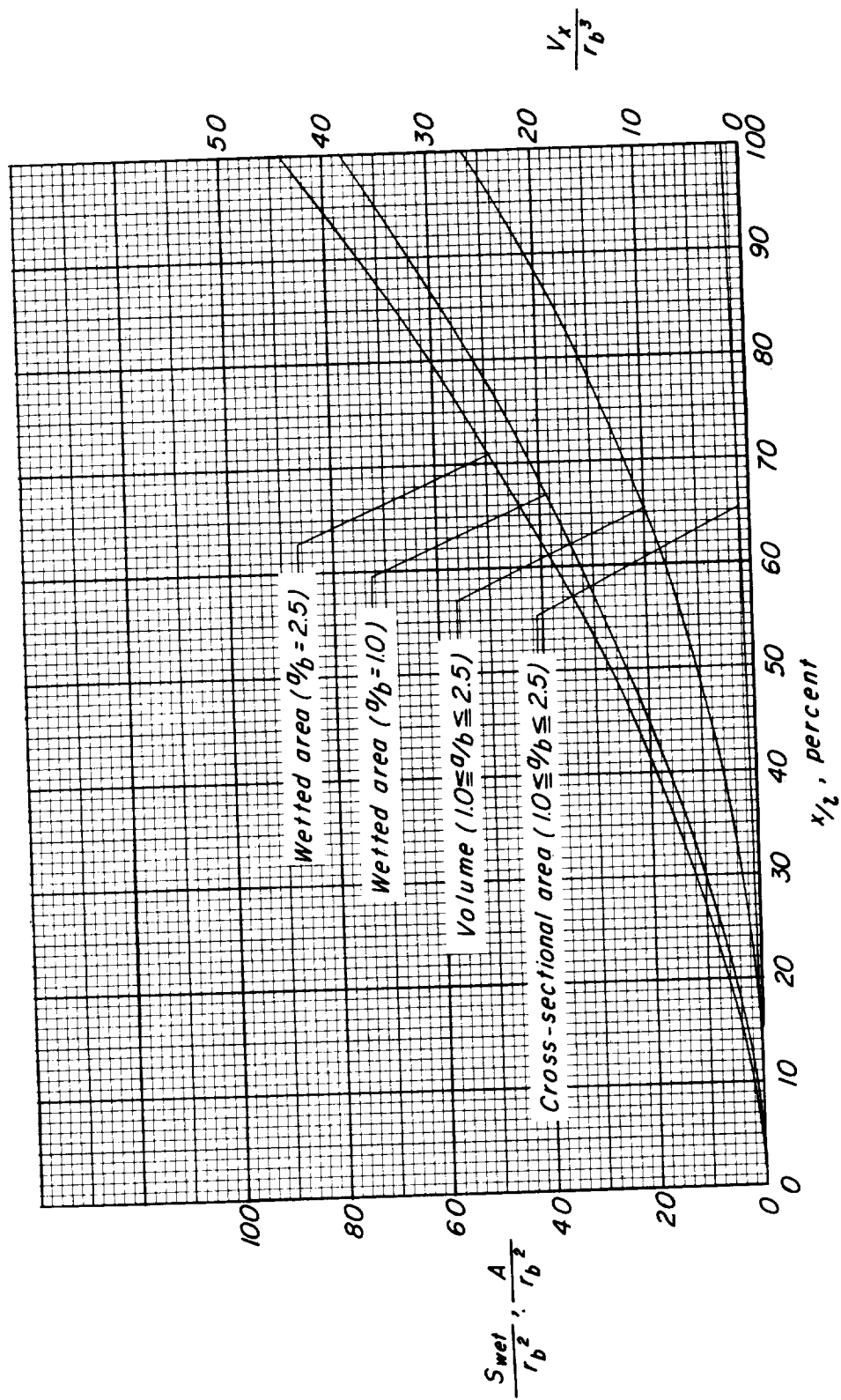
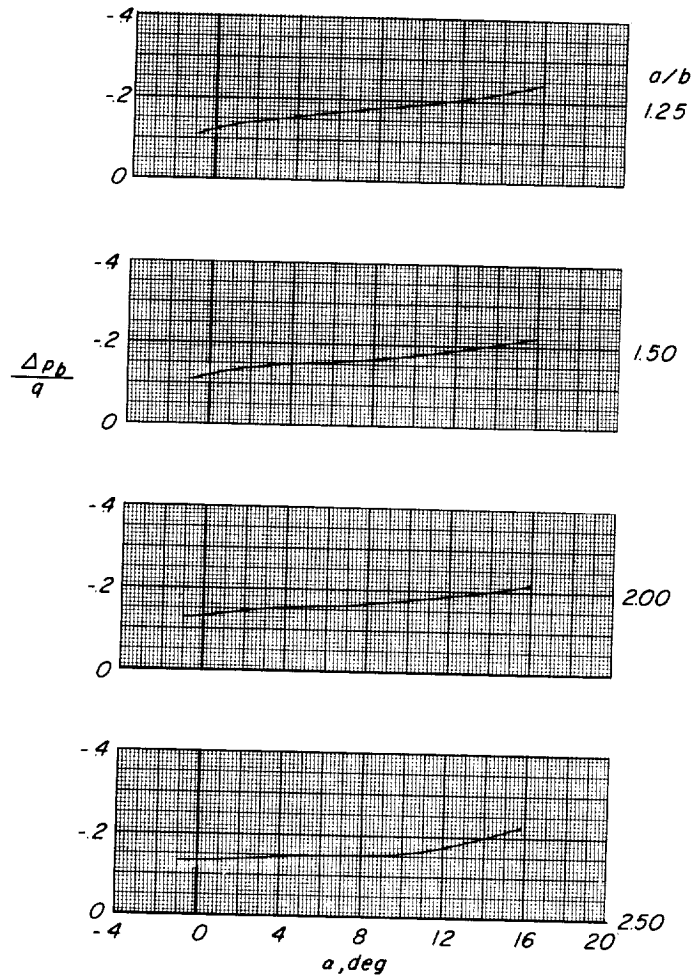
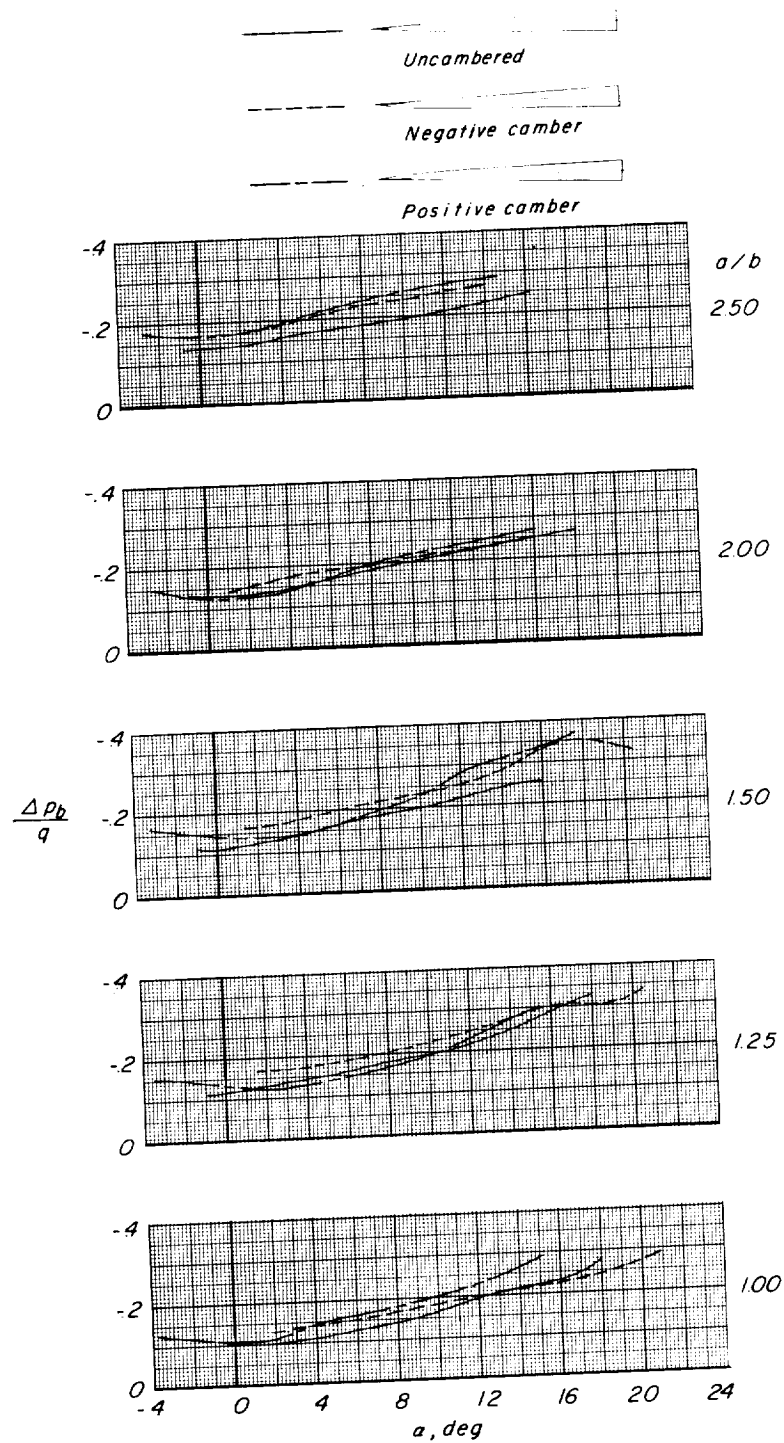


Figure 3.- Variation of volume, cross-sectional area, and wetted area distributions with body length. $a/b = 1.00$ and 2.50 .



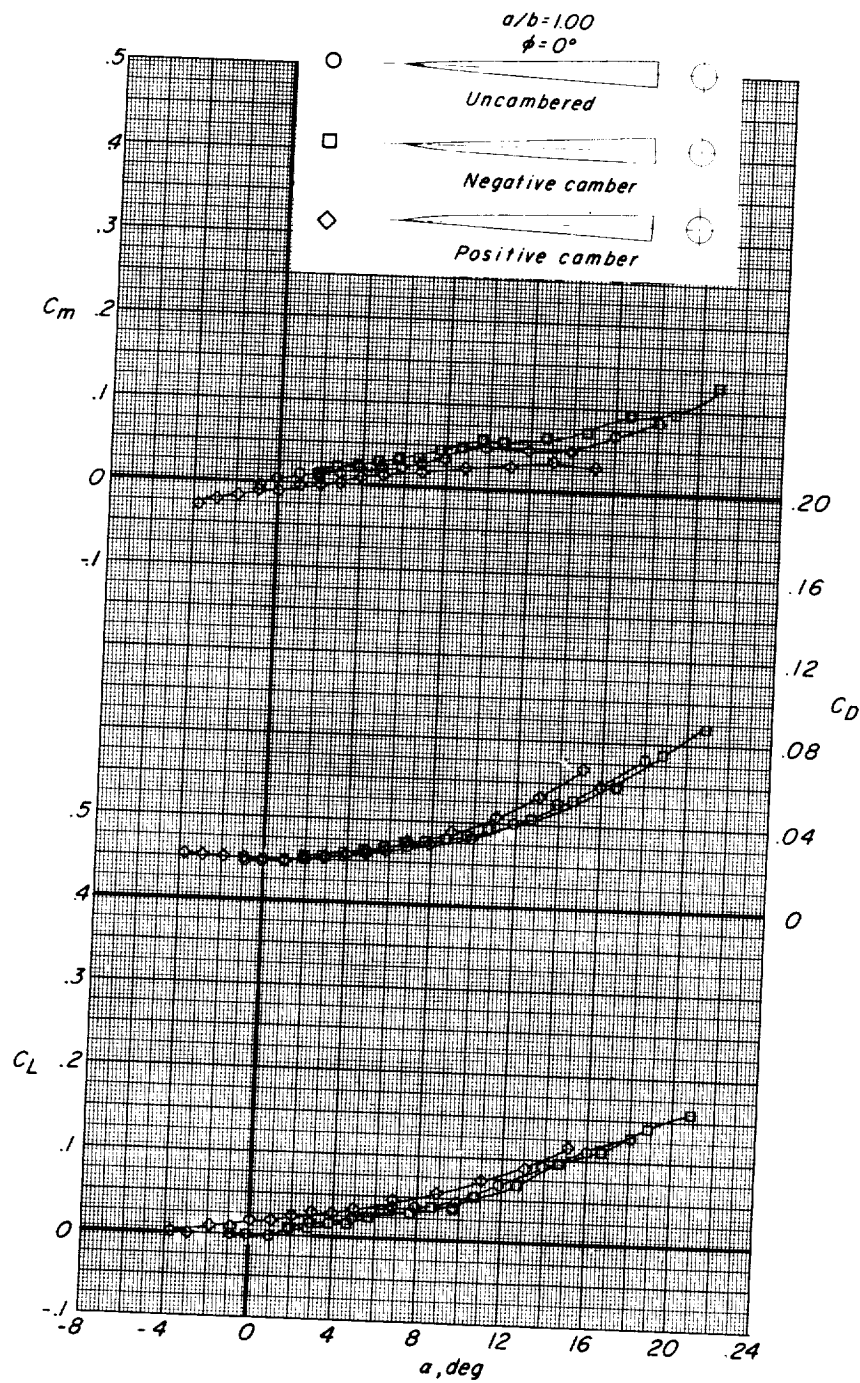
(a) $\phi = 90^\circ$; uncambered bodies.

Figure 4.- Base pressure coefficient variation with angle of attack for various bodies of investigation.



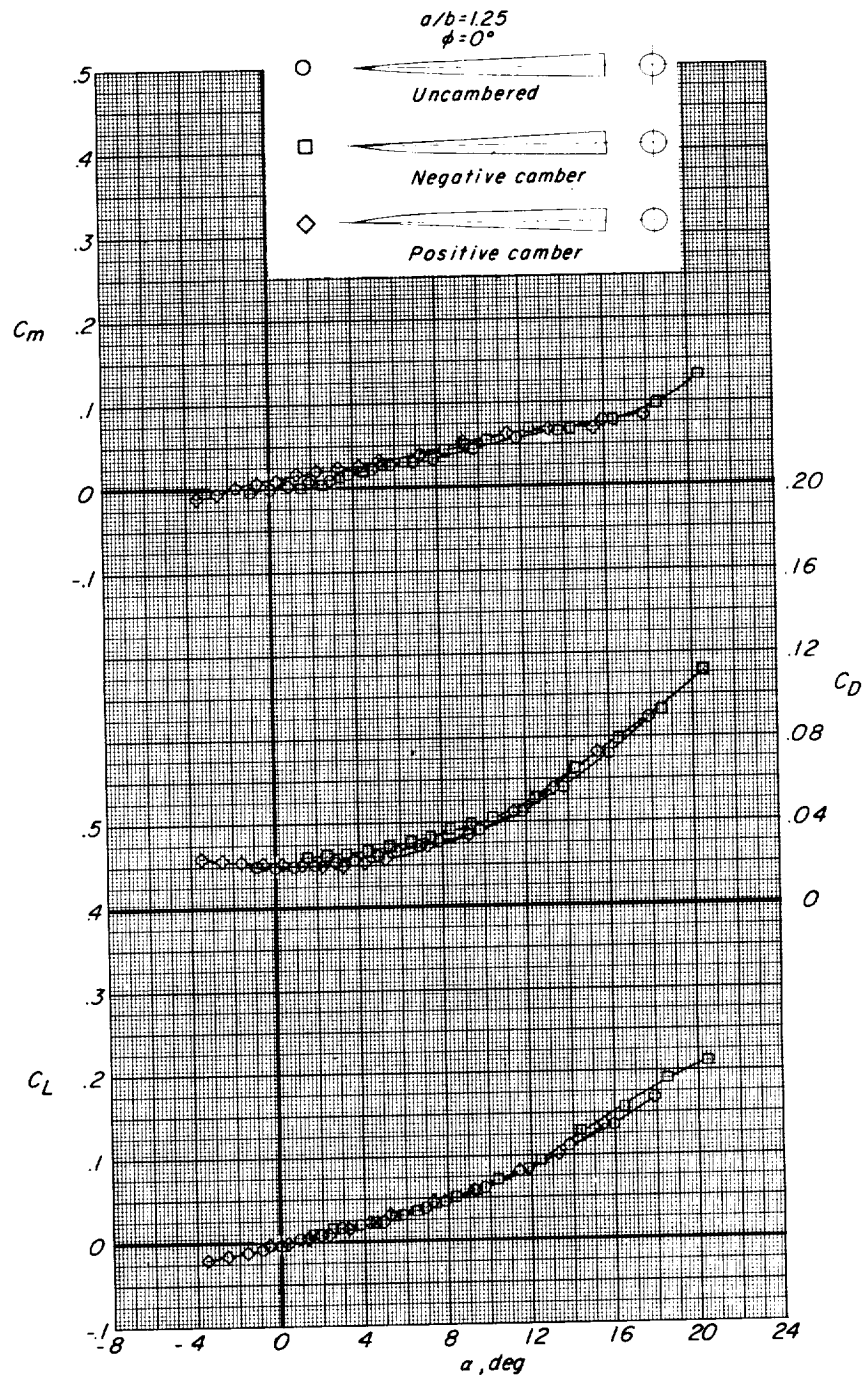
(b) $\phi = 0^\circ$.

Figure 4.- Concluded.



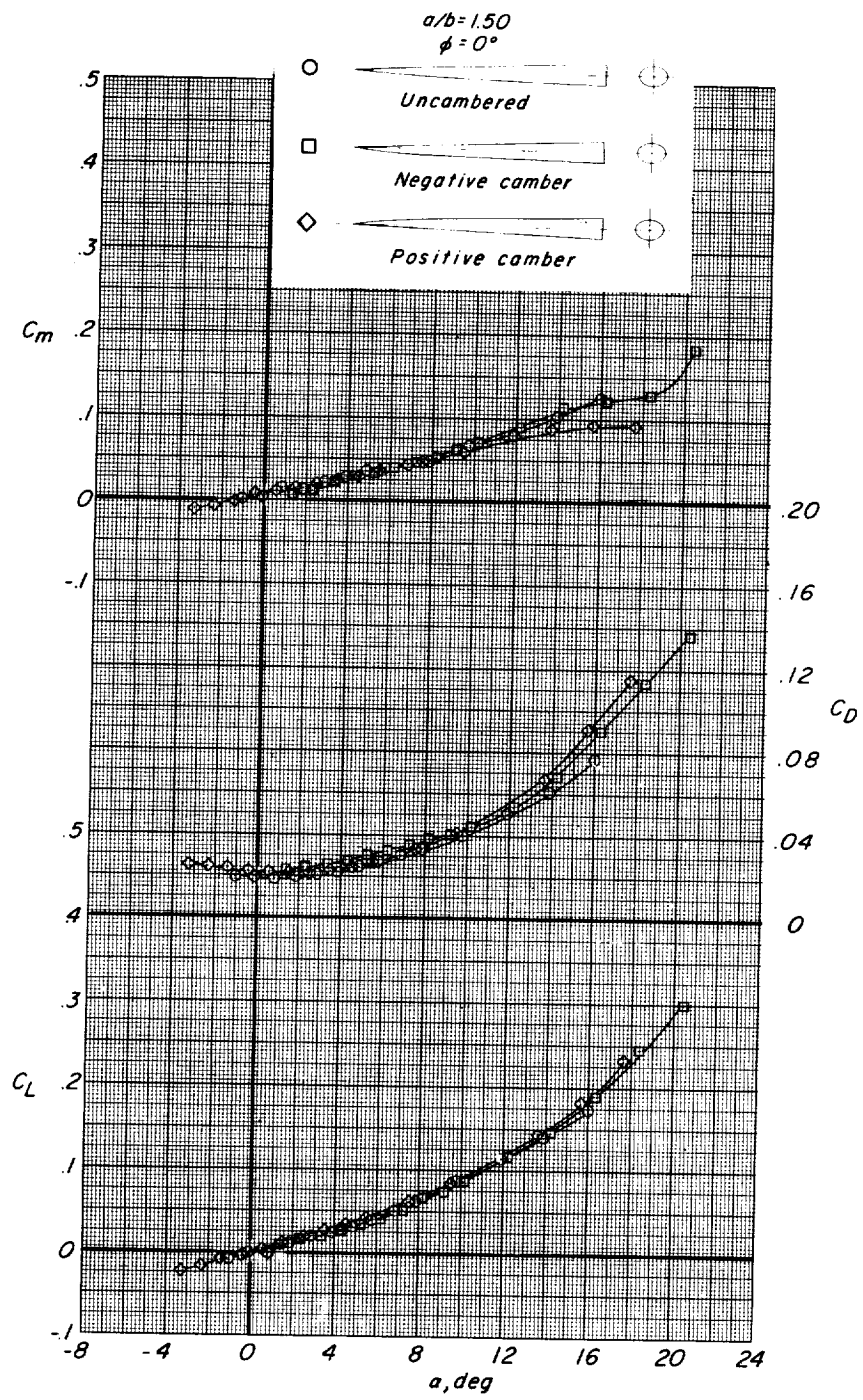
(a) $a/b = 1.00$.

Figure 5.- Effect on longitudinal aerodynamic characteristics of positive and negative camber for bodies having fineness ratio 10.00 and variation in a/b from 1.00 to 2.50. $\phi = 0^\circ$; $\beta = 0^\circ$.



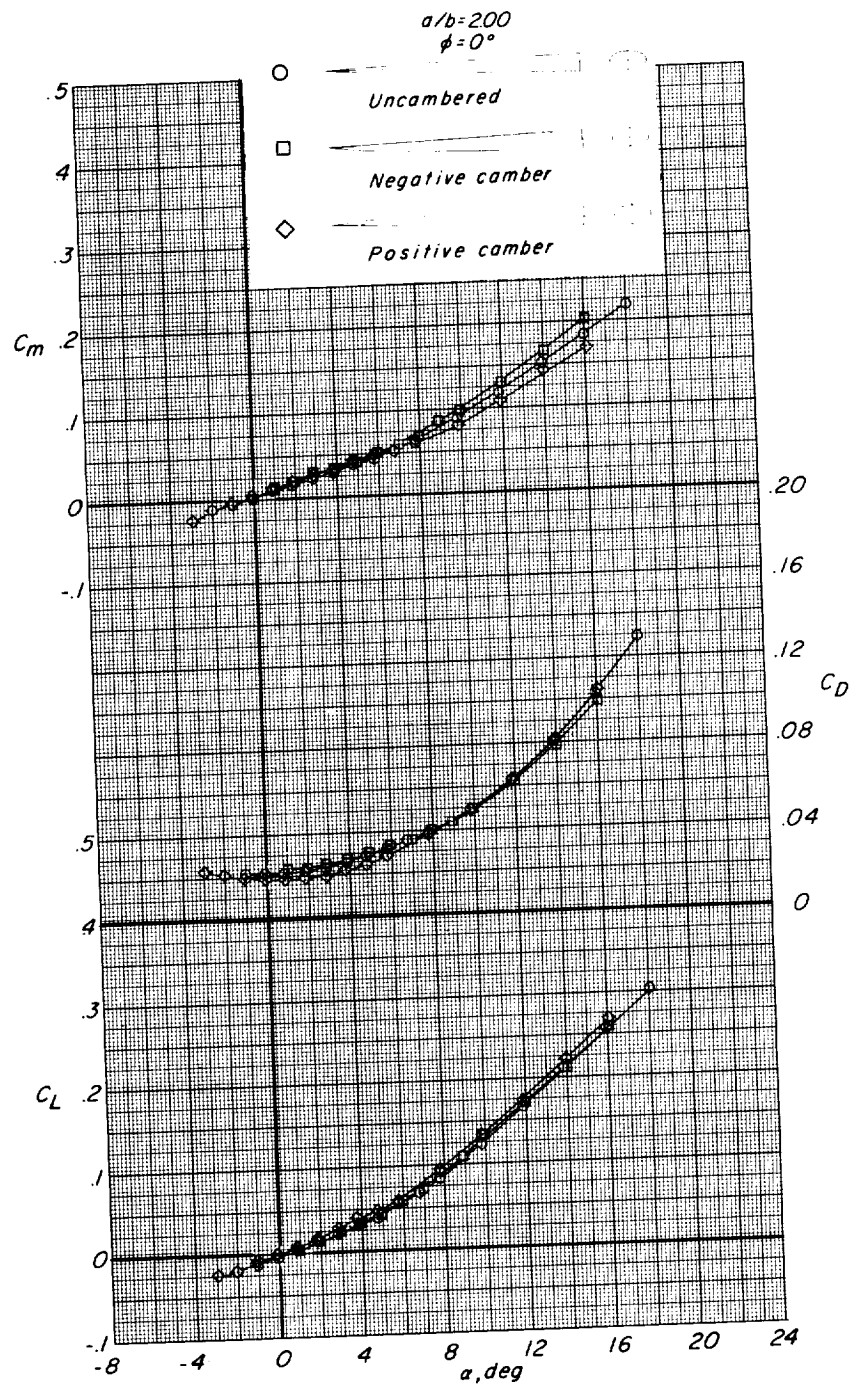
(b) $a/b = 1.25$.

Figure 5.- Continued.



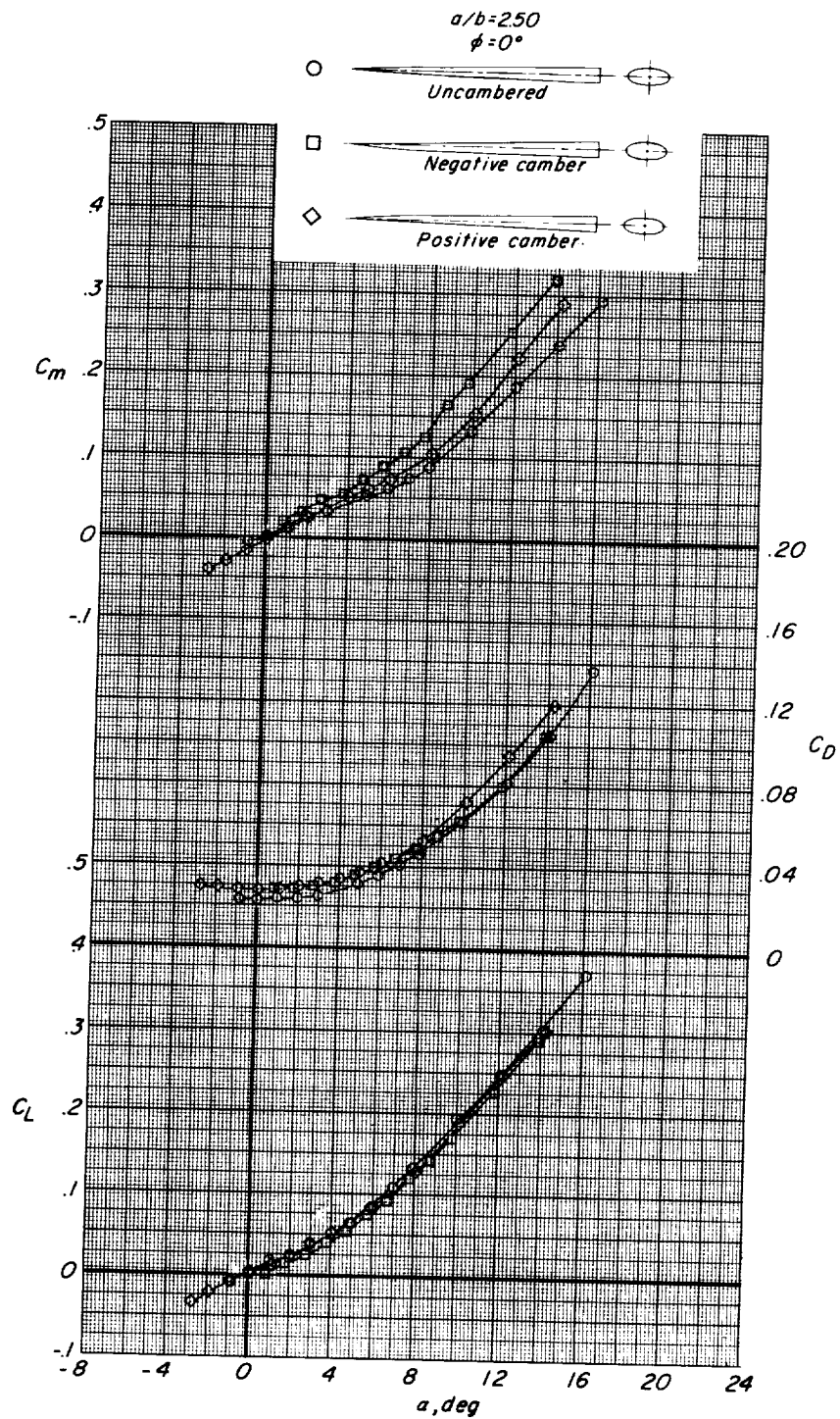
(c) $a/b = 1.50$.

Figure 5.- Continued.



(d) $a/b = 2.00$.

Figure 5.- Continued.



(e) $a/b = 2.50$.
Figure 5.- Concluded.

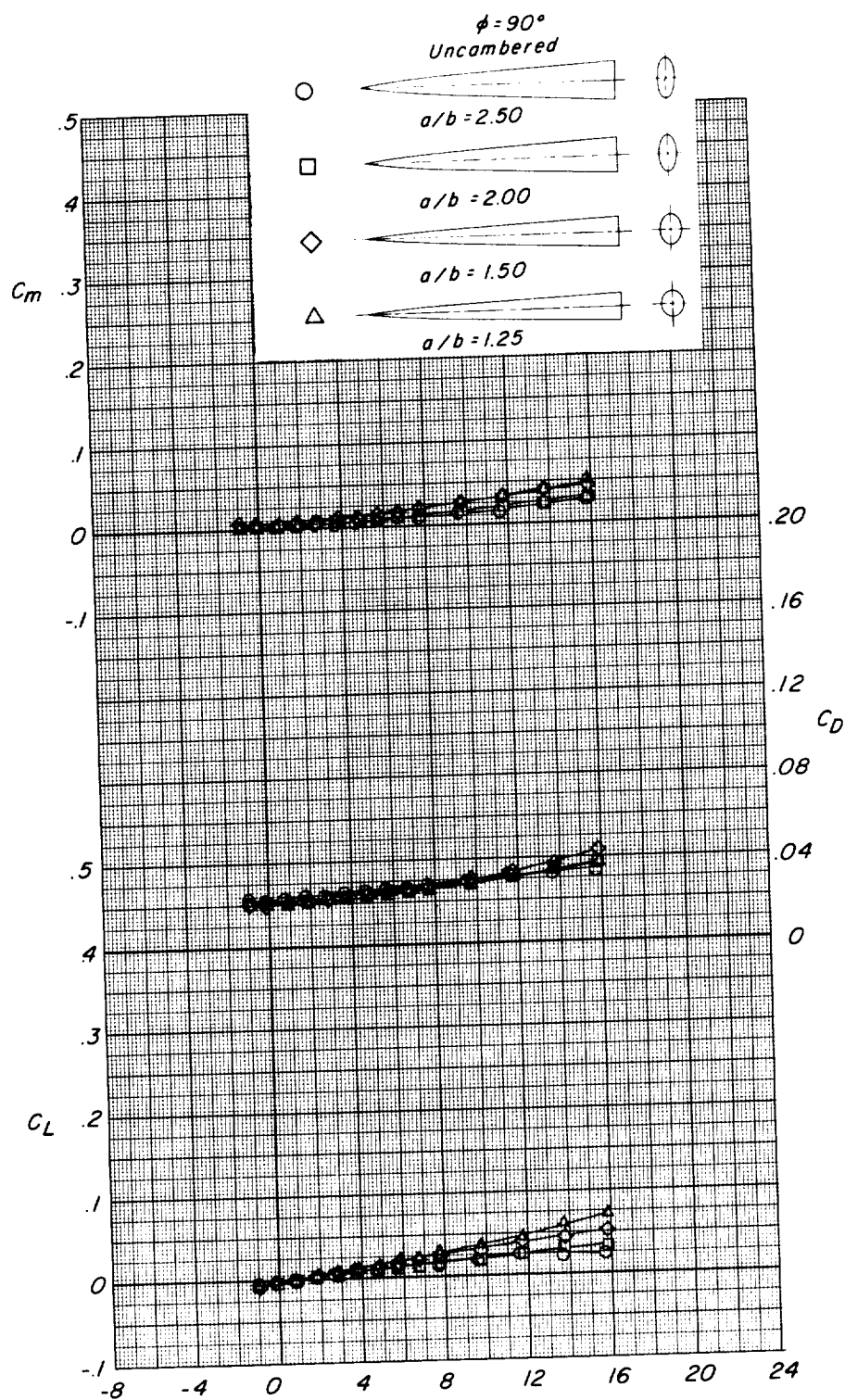
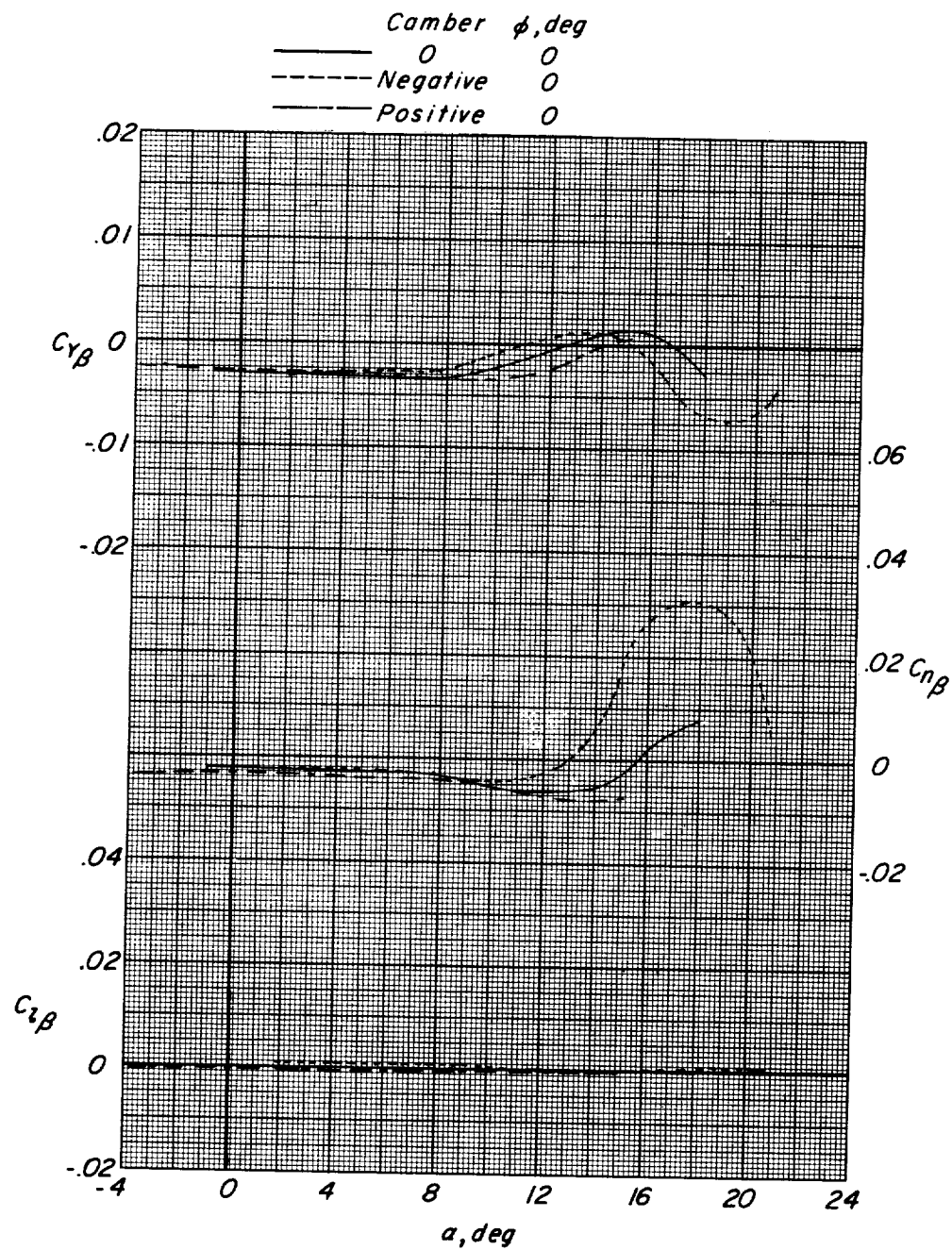
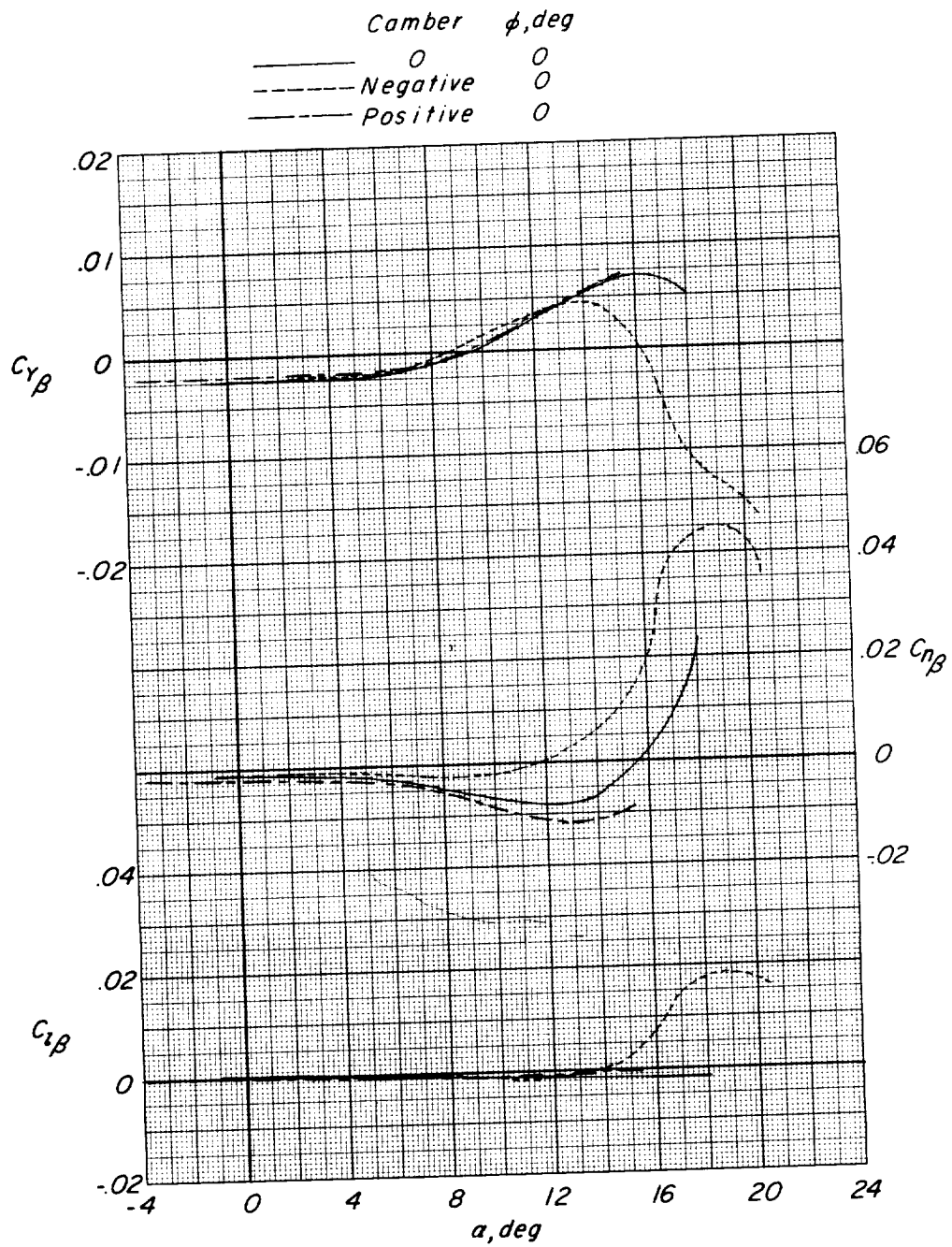


Figure 6.- Effect on longitudinal aerodynamic characteristics of changing a/b from 2.50 to 1.25 at $\phi = 90^\circ$ for the uncambered bodies having fineness ratio 10.00.



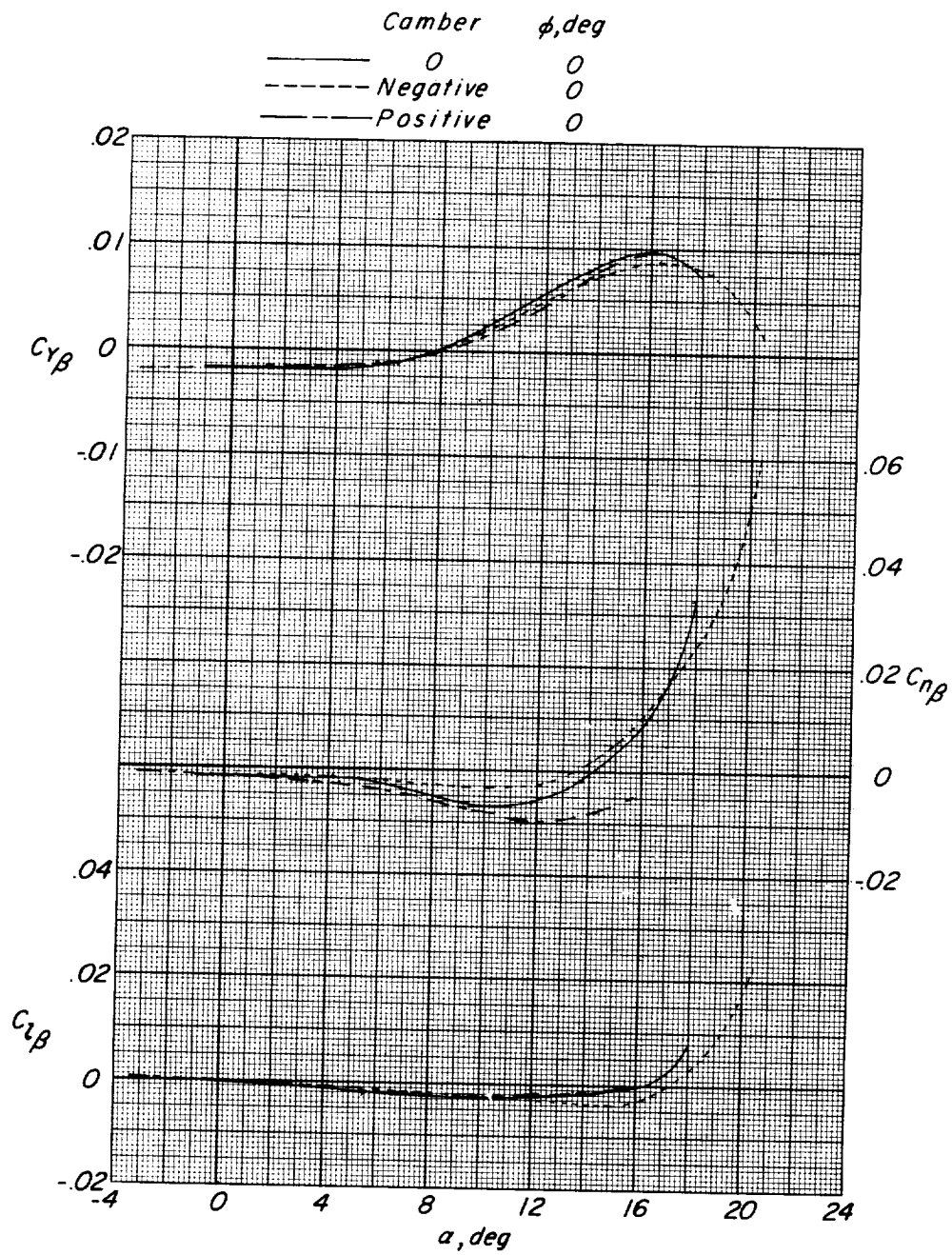
(a) $a/b = 1.00$.

Figure 7.- Effect of positive and negative camber on variation of lateral directional stability derivatives with angle of attack for bodies having fineness ratio 10.00 and a/b from 1.00 to 2.50 at $\phi = 0^\circ$.



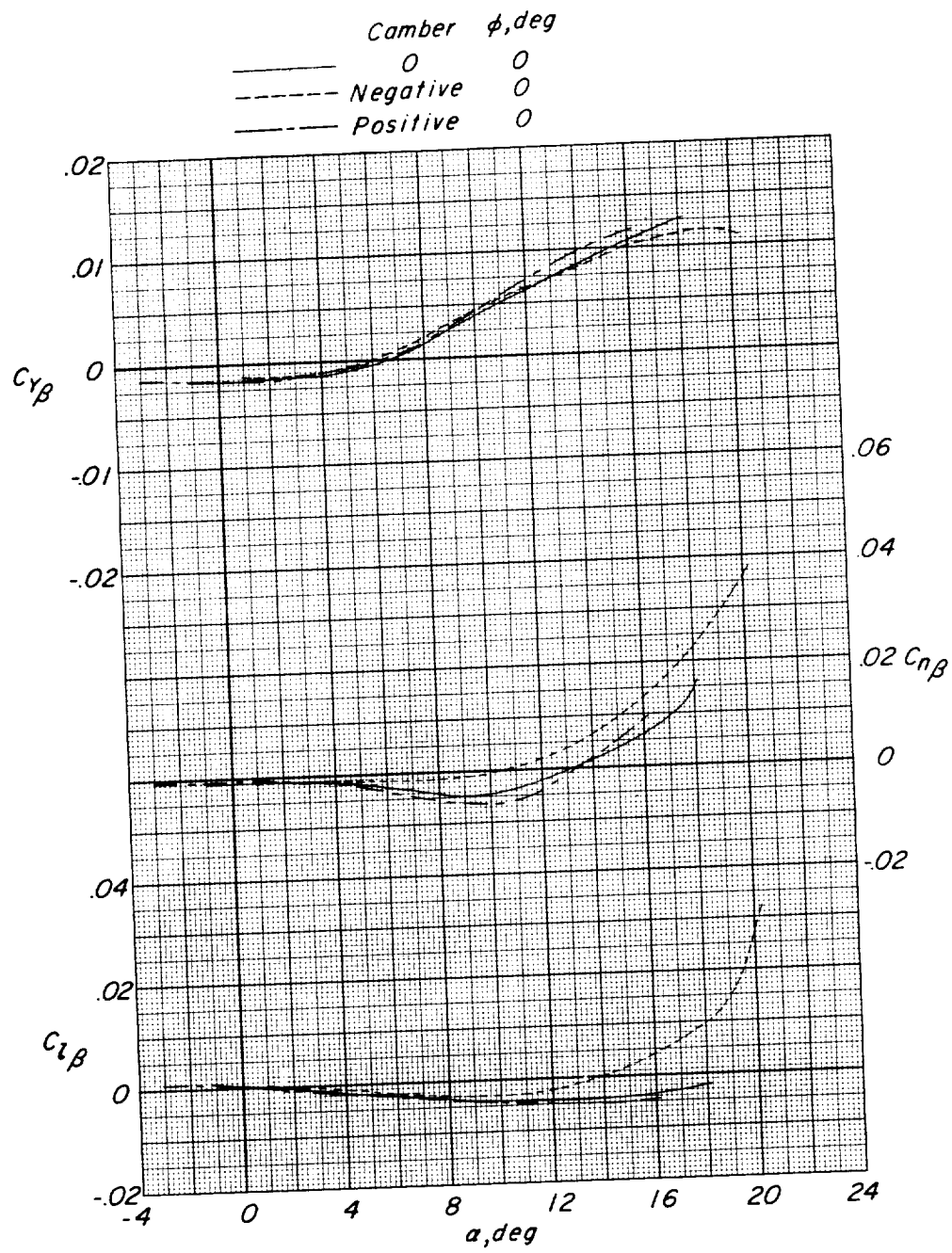
(b) $a/b = 1.25$.

Figure 7.- Continued.



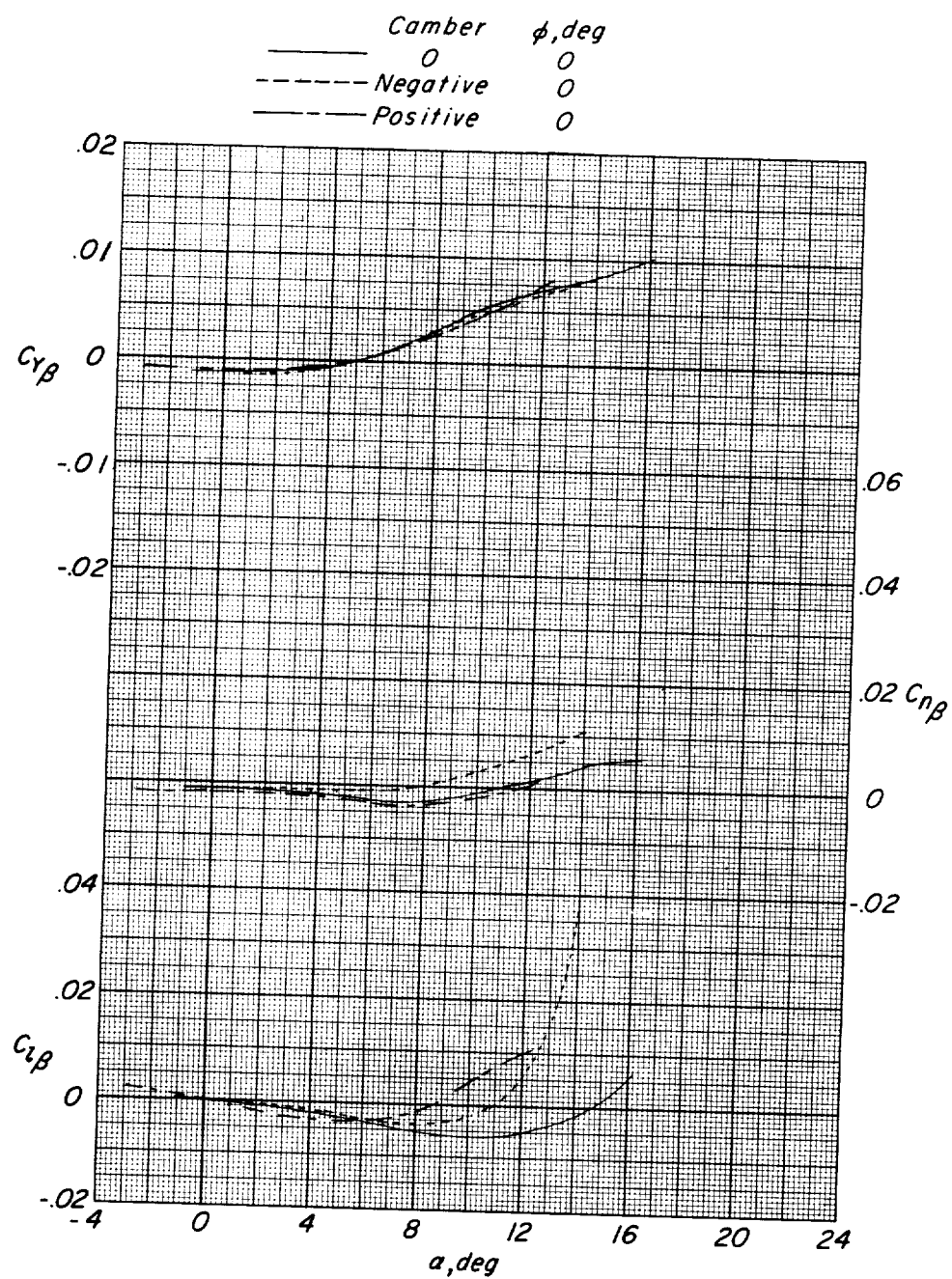
(c) $a/b = 1.50$.

Figure 7.- Continued.



(d) $a/b = 2.00$.

Figure 7.- Continued.



(e) $a/b = 2.50$.

Figure 7.- Concluded.

| | Camber | ϕ, deg | a/b |
|-------|--------|--------------------|-------|
| ———— | 0 | 90 | 2.50 |
| ----- | 0 | 90 | 2.00 |
| ----- | 0 | 90 | 1.50 |
| ----- | 0 | 90 | 1.25 |

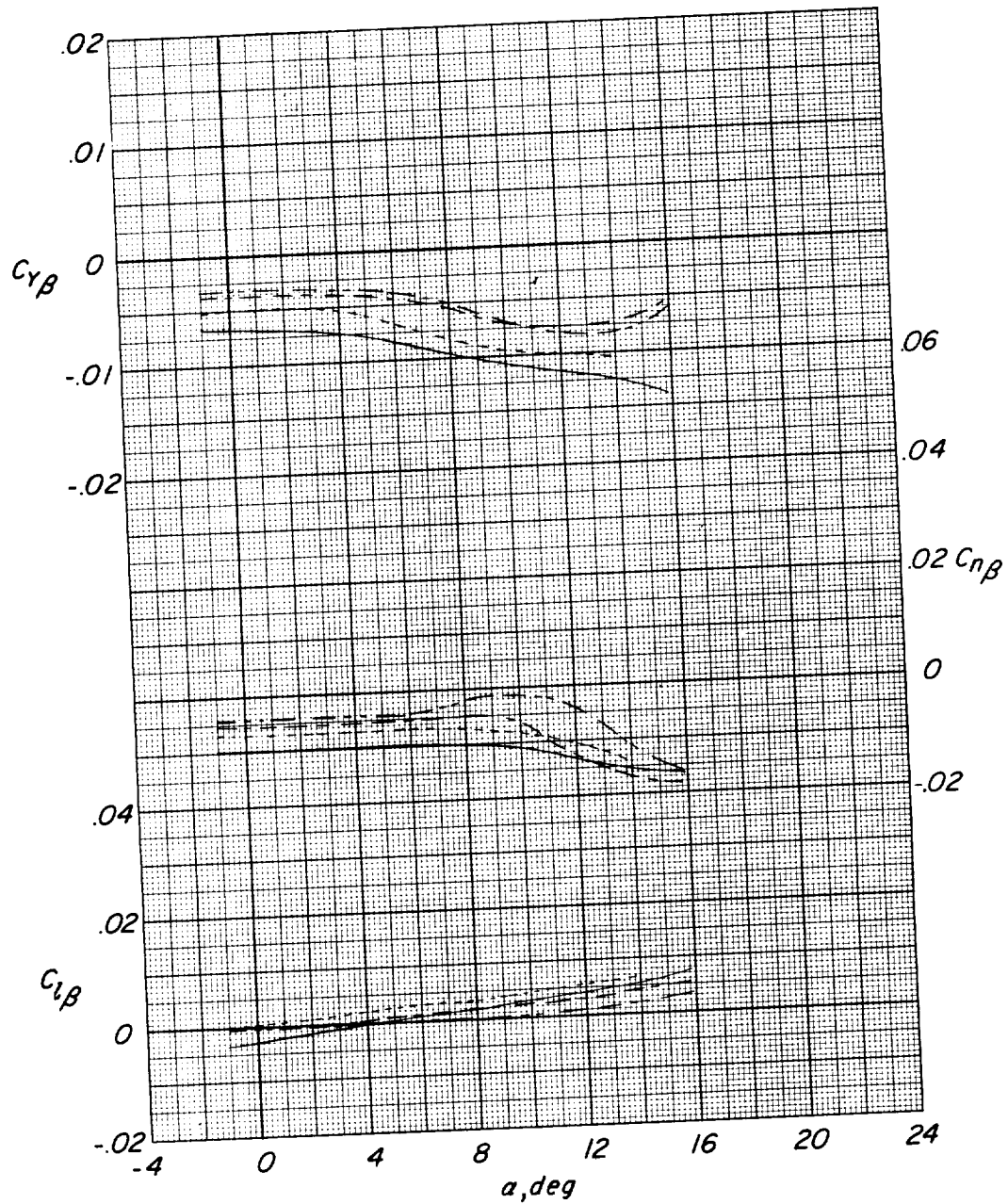
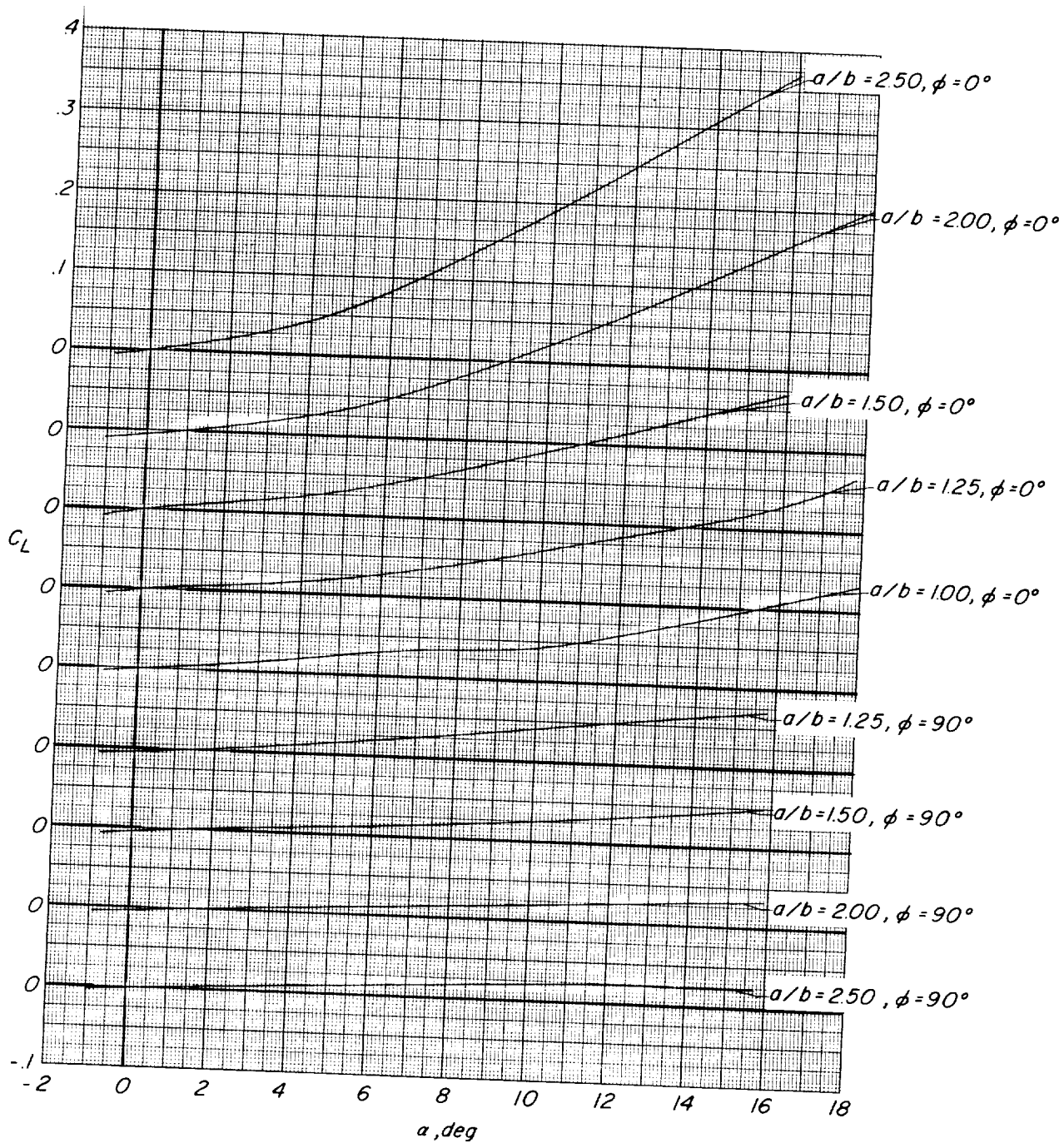
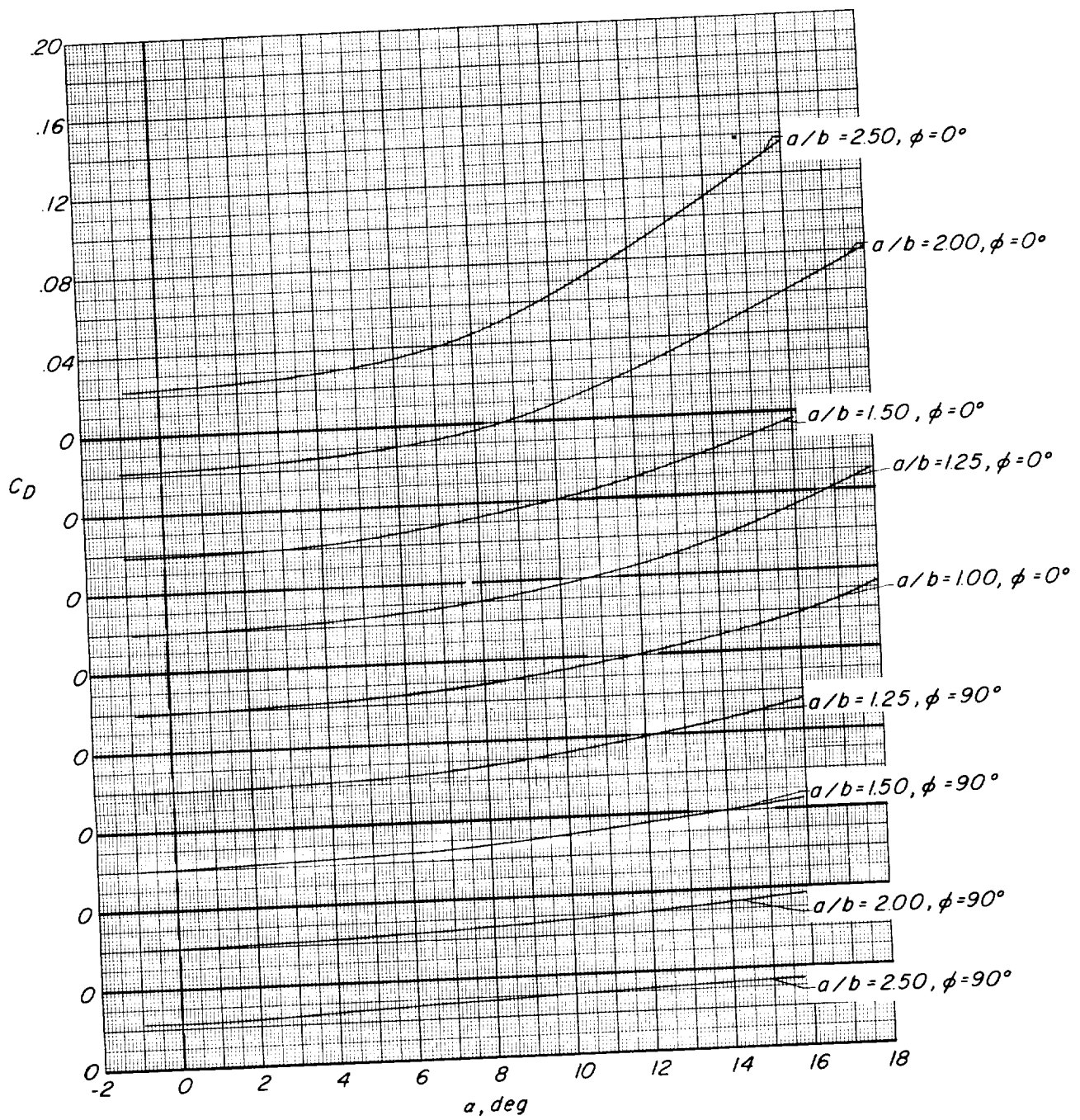


Figure 8.- Effect of changing a/b from 2.50 to 1.00 at $\phi = 90^\circ$ on variation of lateral directional stability derivatives with angle of attack for uncambered bodies having fineness ratio 10.00.



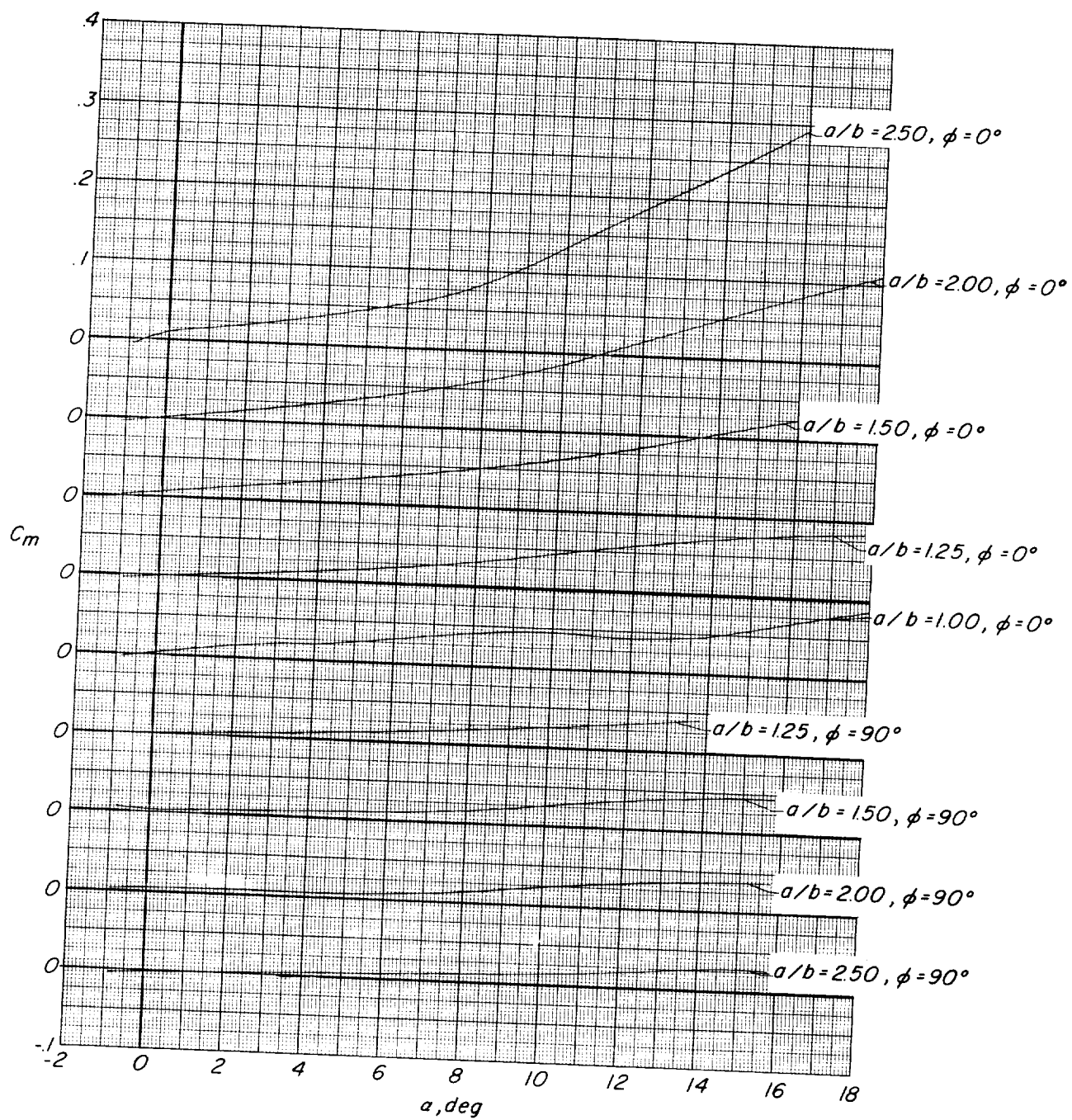
(a) C_L plotted against α .

Figure 9.- Effect on longitudinal aerodynamic characteristics of changing a/b for uncambered bodies having fineness ratio 10.00.



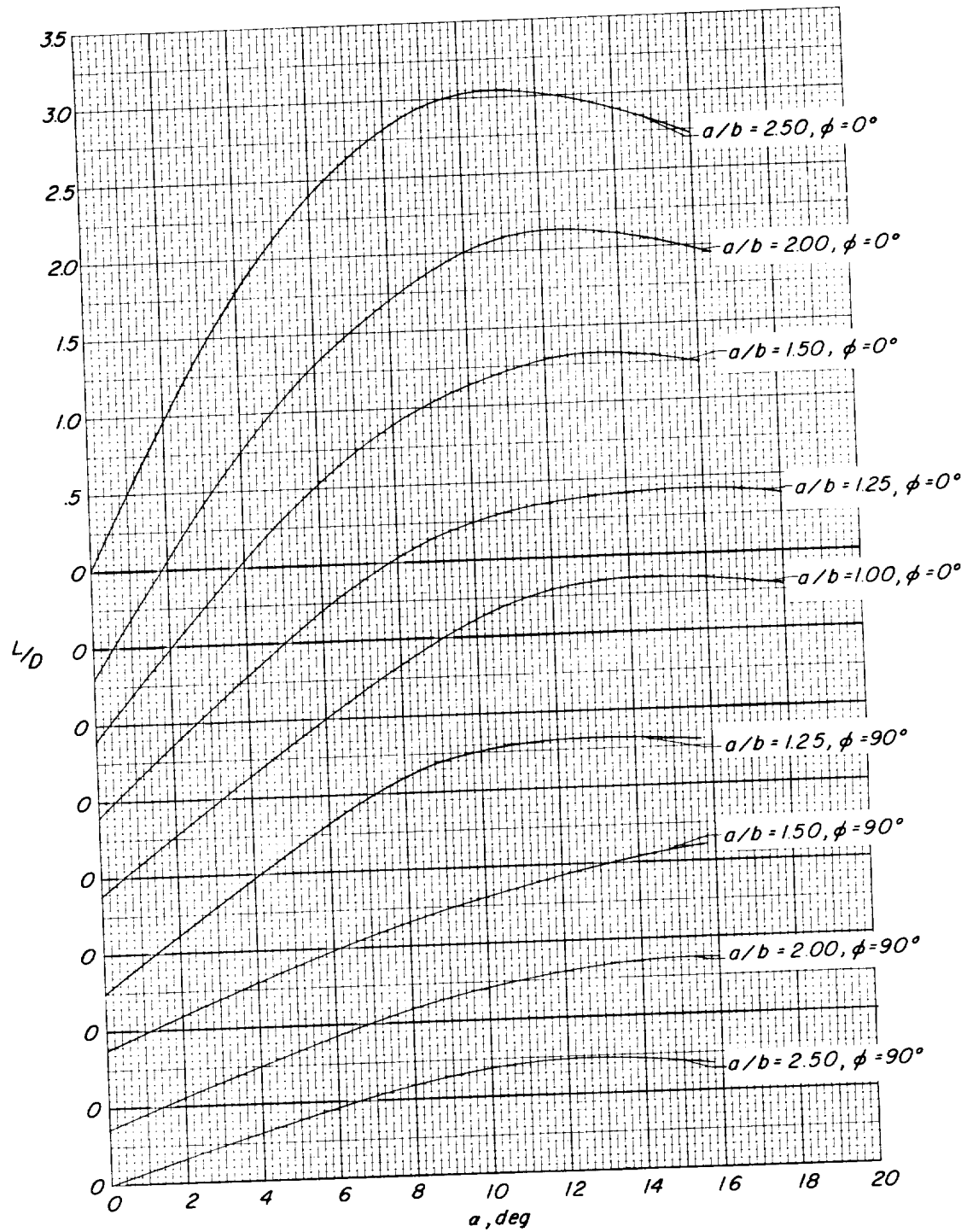
(b) C_D plotted against α .

Figure 9.- Continued.



(c) C_m plotted against α .

Figure 9.- Continued.



(i) L/D plotted against α .

Figure 9.- Concluded.

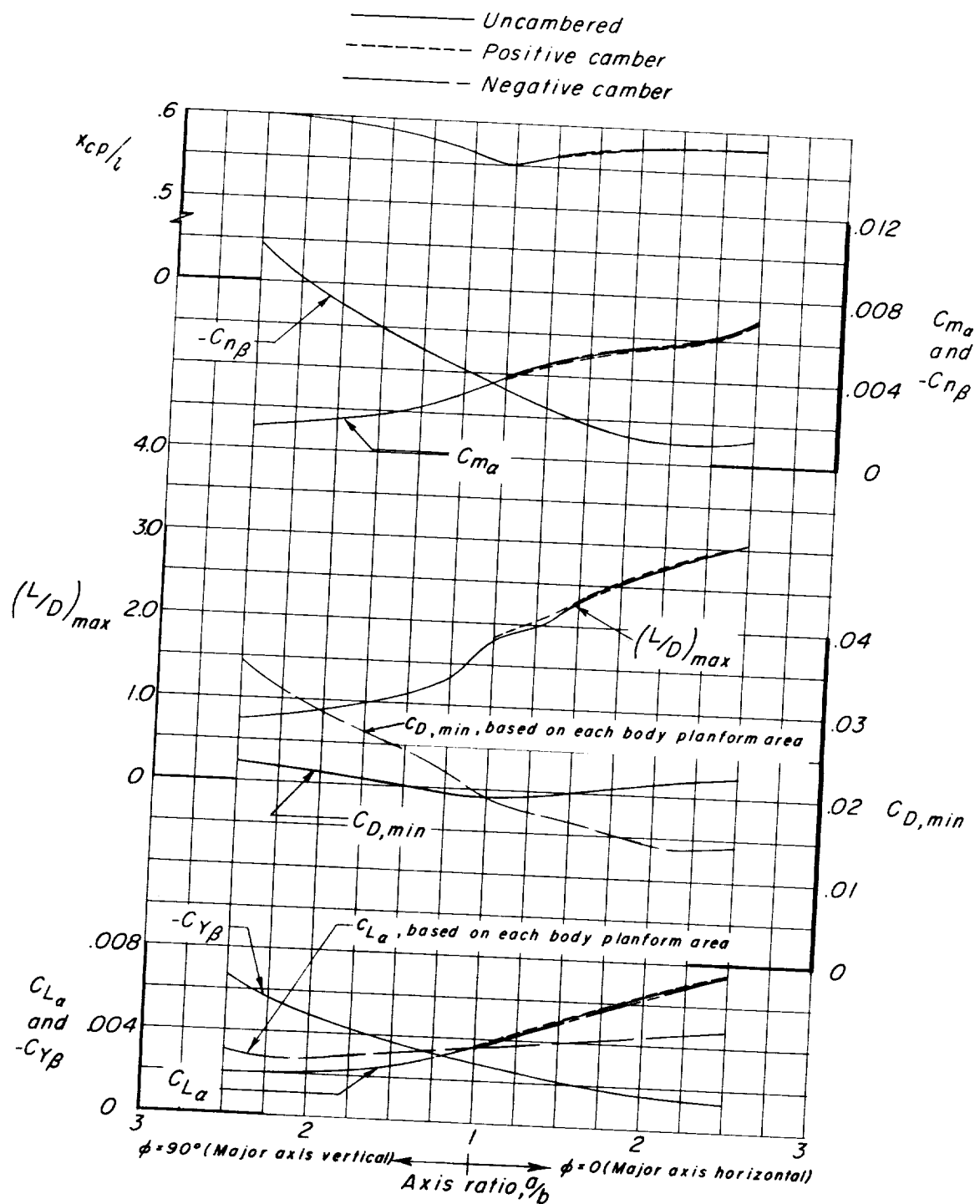


Figure 10.- Summary of longitudinal aerodynamic parameters $C_{L\alpha}$, $C_{D,min}$, $(L/D)_{max}$, $C_{m\alpha}$, and $\frac{x_{cp}}{l}$, for various values of a/b .
